Static morphogen scaling enables proportional growth in tissue growth model inspired by axolotl limb regeneration

Natalia Lyubaykina[a], Dunja Knapp[b,c,1], Pietro Tardivo[d], Tatiana Sandoval-Guzmán[b,e,c,1], and Benjamin M. Friedrich[a,1]

[a]Cluster of Excellence 'Physics of Life', TU Dresden, Dresden, Germany

[b]Department of Internal Medicine III, University Hospital Carl Gustav Carus, TU Dresden, Dresden, Germany
[c]Paul Langerhans Institute Dresden, Helmholtz Centre Munich at TU Dresden, Dresden, Germany

[d]Institute of Molecular Biotechnology of the Austrian Academy of Sciences (IMBA), Vienna BioCenter (VBC), Vienna, Austria
[e]Center for Regenerative Therapies Dresden, TU Dresden, Dresden, Germany

Axolotls can regenerate lost limbs throughout their lives, while they continue to grow. This poses the question of how the size and pattern of a regenerating limb is matched to a widely varying animal size. Two interacting signaling molecules, SHH and FGF8, are produced at opposite sides of the regenerating limb and sustain tissue growth through a pair of oppositely-oriented signaling gradients. As the size of the regrowing tissue can vary more than three-fold depending on the size of the animal, it is unclear how the activities of these mutually dependent morphogens are maintained and subsequently terminated to determine appropriate growth. Scaling of limb regeneration suggests a size-dependent adaptation of morphogen gradient parameters. Inspired by this biological example, we theoretically investigate general mechanisms of morphogen-controlled growth arrest and proportional growth. In the proposed mechanism, tissue growth increases the spatial distance between the two morphogen gradients, thus providing negative feedback that eventually arrests morphogen activity and growth. We put forward two distinct scaling scenarios of morphogen gradients: either dynamic scaling with blastema size, where morphogen gradient parameters change dynamically with the growing tissue, or static scaling with animal size, where morphogen gradient parameters stay constant during blastema growth and only depend on animal size. We show that static scaling ensures proportional growth, but dynamic scaling does not. We compare theory predictions to experimental quantification of SHH and FGF8 morphogen gradient parameters at different time-points of regeneration in different-sized animals, indicating static scaling for some morphogen parameters, which is sufficient to ensure proportional growth in our model.

regeneration | axolotl | adaptive morphogenesis | growth control | morphogen gradient scaling

Correspondence: *benjamin.m.friedrich@tu-dresden.de, tatiana.sandoval_guzman@tu-dresden.de, dunja.knapp@tu-dresden.de*

Introduction

Axolotls possess remarkable regenerative capabilities, including the ability to regenerate fully functional limbs even in adulthood (Dinsmore, 2004). Limb regeneration shares similarities with limb development (Muneoka and Bryant, 1982; Payzin-Dogru and Whited, 2018), which is largely conserved among vertebrates (Young and Tabin, 2017). However, limb regeneration must also cope with the different sizes of juvenile and adult animals, which can differ up to ten-fold in linear size (Vieira et al., 2020). Regeneration to match animal size represents a general open problem of adaptive morphogenesis (Leigh and Currie, 2022). Limb regeneration in axolotls starts with wound closure after limb loss, followed by the formation of a bud called blastema consisting of undifferentiated progenitor cells, growth of this blastema, and eventually cell differentiation to give rise to various limb tissues (Fig. 1B). The result of this first phase of blastema growth is a hypometric limb (called "tiny limb" in (Wells et al., 2021)), whose size scales allometrically with animal size (Furukawa et al., 2024), (see also Supporting Information (SI), Fig. S1). This hypometric limb subsequently grows to its final size in a second growth phase, which is particularly pronounced in larger animals (Wells et al., 2021). The first growth phase of limb regeneration, which we refer to as *blastema growth*, is shown in

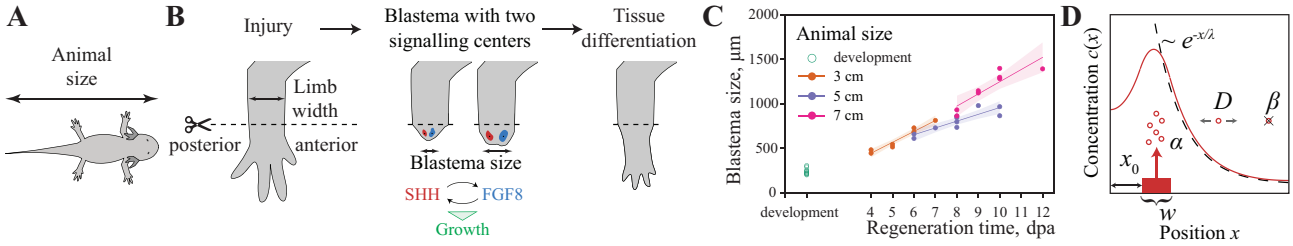

Figure 1. *Axolotl limb regeneration. A.* Schematic of an axolotl, with definition of snout-to-tail animal size. *B.* Schematic of axolotl limb regeneration, highlighting its key stages: After limb amputation, a blastema with two distinct signaling centers comprising SHH posteriorly (red) and FGF8 anteriorly (blue) forms. These mutually reinforcing morphogens induce cell proliferation, and thus regulate blastema growth. After this first growth phase of blastema growth, tissue differentiation and additional growth completes limb regeneration. Dashed line indicates amputation plane, arrows indicate limb and blastema size. *C.* Blastema size at subsequent time points (days post amputation, dpa) for animals of different size (filled symbols), and development (open symbols; measured along a line passing through the centers of *Shh* and *Fgf8* regions in 3D images, for details see Methods). *D.* Morphogen gradient described by minimal reaction-diffusion model Eq. (1) together with visualization of model parameters.

Fig. 1C (wide-field images of corresponding stages are shown in SI appendix, Fig. S2). Blastema growth involves a pair of oppositely-oriented morphogen gradients. Like the developing limb bud, the regenerating blastema display two signaling centers that secrete morphogens: a posterior center expressing SHH (Sonic Hedgehog) (Torok et al., 1999; Tickle and Towers, 2017), and an anterior center expressing FGF8 (Fibroblast Growth Factor) (Han et al., 2001; Purushothaman et al., 2019), which mutually reinforce each other's expression (Laufer et al., 1994; Niswander et al., 1994; Bénazet et al., 2009). In intact mature limbs, SHH and FGF8 are undetectable (Otsuki et al., 2023; Nacu et al., 2016) (see also Fig. S3 in SI appendix). However, following injury, their production is activated, with clear evidence that both SHH and FGF8 are essential for maintaining blastema growth and successful limb regeneration (Nacu et al., 2016; Han et al., 2001; Torok et al., 1999). Because of their mutual feedback, the individual roles of SHH and FGF8 in regulating cell proliferation are challenging to disentangle. While neither morphogen alone seems sufficient to support growth and regeneration in ectopically induced blastemas *in vivo* (Nacu et al., 2016), both enhance proliferation individually and additively in cultured dissociated blastema cells *in vitro* (Furukawa et al., 2024). Consequently, it remains challenging to determine whether one or both morphogens directly up-regulate proliferation.

Here, we focus on the stage of blastema growth as a paradigmatic model system for morphogen-dependent growth control and growth arrest in animals of different sizes. Recently, the sizes of the source regions of SHH and FGF8 were measured by chromogenic RNA *in situ* stainings in thin sections of middle-stage blastemas of animals of different sizes, indicating allometric scaling of source regions with animal size at the chosen time-point (Furukawa et al., 2024). Inspired by this, we explore a minimal mathematical model of coupled tissue growth and morphogen dynamics in a system of two morphogens to identify physical mechanisms that ensure robust growth arrest and proportional growth. We systematically dissect differences between two fundamental growth rules based on either one or two morphogens, as well as two scaling scenarios of morphogen gradients, scaling either *dynamically* with growing blastema size, or *statically* with animal size. Our theoretical analysis singles out a mechanism of growth control by two oppositely-oriented morphogen gradients, where at least some morphogen gradient parameters must exhibit static scaling to enable proportional growth. By combining whole mount *in situ* hybridization with tissue clearing and confocal microscopy (Glotzer et al., 2022), we quantify the three-dimensional size of SHH and FGF8 morphogen sources as function of time in regenerating blastemas of different-sized animals, as well as the FGF8 signaling range by measuring the expression of its down-stream target *Dusp6*. We found that some gradient parameters (FGF8 source size) scale *statically* with animal size, while others scale *dynamically* with blastema size. Such scaling is sufficient to ensure proportional growth in our model.

Results

Coupling morphogen dynamics and growth

As a minimal model of morphogen dynamics in a growing blastema, we consider a one-dimensional system of size L, see Fig. 1D. We first introduce notation for the simple case of a single morphogen. The morphogen is produced within a source region of width w (located at a distance x_0 from the tissue boundary), subsequently diffuses through the tissue with effective diffusion coefficient D, while undergoing degradation with degradation rate β. The dynamics of morphogen concentration $c(x,t)$ as function of time t is then given by

$$\partial_t c(x,t) = D\,\partial_x^2 c(x,t) - \beta c(x,t) + \alpha\,\chi_w(x) \quad . \tag{1}$$

Here, the source function $\chi_w(x)$ characterizes the shape of the morphogen source, which we assume to take the value 1 inside the interval $[x_0, x_0+w]$ and zero outside. The rate total of morphogen production is thus $j = \alpha w$, with units of molecules per time. The steady-state morphogen concentration profile $c^*(x)$ that is established at long times is thus fully defined by five parameters, which set its amplitude A and a characteristic pattern length-scale λ. This pattern length-scale is determined by a competition between the diffusion coefficient D and the degradation rate β

$$\lambda = \sqrt{\frac{D}{\beta}} \quad . \tag{2}$$

The steady-state concentration gradient $c^*(x)$ approximately follows an exponentially decaying profile with this pattern length-scale λ

$$c^*(x) \approx \frac{\alpha w}{\sqrt{D\beta}} \exp\left(-\frac{x}{\lambda}\right) \quad . \tag{3}$$

This approximation becomes exact when the morphogen source is small, localized on the system's boundary, and the system is large. Analytic formulas for more realistic cases are given in SI appendix, Eq. (S17). Generally, concentrations are higher in smaller, bounded systems, as morphogens spread in a smaller domain. This size-dependence of morphogen concentrations will become important in our model, once morphogens control growth.

Eq. (1) generalizes in a straightforward manner to the case of two morphogens with respective concentration fields $s(x,t)$ and $f(x,t)$ instead of $c(x,t)$ in Eq. (1), where $s(x)$ and $f(x)$ can be thought of as the concentrations of SHH and FGF8 morphogens. For conceptual clarity, we consider a symmetric case of two morphogens with identical kinetic parameters and mirror-symmetric source regions (see SI appendix, Eqs. (S21-S22) for their formulas analogous to Eq. (1)). The general case of not-identical parameters for two morphogens is qualitatively similar.

To address the dynamics in growing tissue, we consider a one-dimensional tissue that grows with local growth rate $g(x,t)$. Tissue growth convects the concentration field $c(x,t)$ of morphogen with velocity $v(x,t)$ where $\partial_x v = g$, as well as dilutes local morphogen concentration at rate g (see Methods).

Growth control by one or two morphogens

Two interacting morphogens, SHH and FGF8, are implicated in regulating cell proliferation in axolotl limb development and regeneration (Furukawa et al., 2024; Nacu et al., 2016). Due to the mutual feedback between these two morphogens, inactivating one consequently inactivates the other. Therefore, it is experimentally difficult to determine if the direct signal from just one or from both morphogens is needed to promote proliferation. To theoretically explore both cases, we define two putative growth rules, both of which are inspired by a switch-like control of cell behavior as function of local morphogen concentration (Wolpert, 1969). Specifically, we assume that the tissue grows locally if morphogen concentrations are above a threshold:

One-morphogen growth rule: the tissue grows at the position x if (and only if) the concentration $c(x)$ of a morphogen is above a fixed threshold Θ, see Fig. 2A.

Two-morphogen growth rule: the tissue grows at the position x if the concentrations of both morphogens, $s(x)$ and $f(x)$ (e.g., SHH and FGF8) are above a fixed threshold Θ, see Fig. 2B.

For the sake of simplicity, we assume a symmetric scenario with equal threshold Θ for both $s(x)$ and $f(x)$ for the two-morphogen growth rule. A more general case can be mapped to this special case by a simple rescaling. Source width (w) and position (x_0) are kept constant; more realistic scenarios of source growth are explored in the next section.

We numerically simulated morphogen dynamics according to Eq. (1) coupled with growth for the one- and two-morphogen growth rules introduced above, see Fig. 2. For both growth rules, the amplitudes of the morphogen gradients decrease as the system grows. Consequently, for the one-morphogen growth rule, the growth zone where morphogen levels exceed the threshold ($c(x,t) > \Theta$) shrinks at its border opposite to the source, until – for suitable parameter choices – growth eventually arrests (Fig. 2A). For the two-morphogen growth rule, the growth zone where the levels of both morphogens exceed the threshold ($s(x,t) > \Theta$ and $f(x,t) > \Theta$) shrinks even faster and at both borders, as the two opposing morphogen profiles overlap less when the system grows (Fig. 2B).

Fig. 2C and D show the final system size L^* at growth arrest for the one- and two-morphogen growth rule, respectively. For the one-morphogen growth rule, growth arrests only if the growth threshold Θ exceeds a critical value Θ_c, where $\Theta_c = \alpha w/(D\beta)^{1/2}$ for the limit case of a point source region (for details, see SI appendix, Eq. S25); for $\Theta < \Theta_c$, the system will grow indefinitely (Fig. 2C). For the two-morphogen growth rule, growth always arrests for any threshold (Fig. 2D). Since we consider a source with constant size and position, and the source region should fit into the system, the size of the system should be at least $w + x_0$, setting a minimal size. While we considered an idealized case where growth is slower than the dynamics of the morphogens, implying that morphogen gradients are always in quasi-steady state, numerical simulations reveal qualitatively similar behavior when this assumption

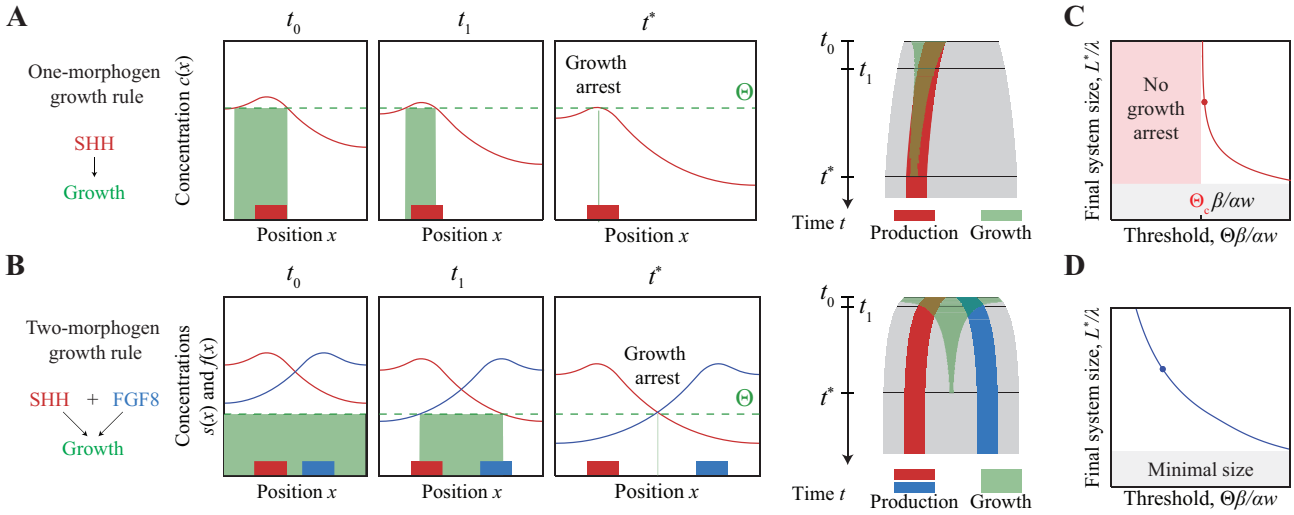

Figure 2. *Two putative growth rules. A.* Schematic of *one-morphogen growth rule*: the tissue grows where the concentration $c(x)$ of a single morphogen is above the growth threshold Θ. Morphogen source region (red region), morphogen gradient (red curve), growth threshold Θ (dashed green line), and growth zone (green region) at different time points. A corresponding kymograph of simulated tissue growth until growth arrest is shown to the right. *B.* Schematic of *two-morphogen growth rule*: a tissue grows only where the concentrations of both morphogens are above the growth threshold Θ. Morphogen gradients (red, blue) of the two morphogens at different time points, analogous to panel A. A kymograph shows production regions of both morphogens (red, blue). *C.* Final system size L^* normalized by pattern length-scale λ as function of a normalized growth threshold $\Theta\beta/\alpha w$ for the one-morphogen growth rule. Θ_c indicates the critical threshold below which the one-morphogen growth rule fails to arrest growth. *D.* Final system size L^* normalized by pattern length-scale λ as function of normalized growth threshold $\Theta\beta/\alpha w$ for the two-morphogen growth rule. Threshold parameter and final system size in panels A and B are indicated by a point in panels C and D, respectively.

is relaxed (SI appendix, Fig. S4). In the SI appendix, we also give analytic formulas for the final system size L^* as a function of the growth threshold Θ for the limit case of a point source region (Eqs. (S24), (S27)). There, we also analyzed the sensitivity of the final system size L^* to the model parameters (Fig. S5), and found that the two-morphogen growth rule is less sensitive to parameter variations and ensures growth arrest for a wider range of parameters. This basic model shows that morphogen-dependent tissue growth can self-terminate, but does not include any scaling. Next, we investigate how tissues can attain the correct, proportionate final size through growth arrest in animals of different sizes.

Dynamic vs. static scaling of morphogen gradients

In the generic model of growth control from the preceding section, the final system size L^* only depends on the initially defined morphogen gradient parameters. In axolotl limb regeneration, the final limb size depends on animal size, suggesting that some parameters of morphogen gradients should be size-dependent. In an idealized scenario of *proportional growth*, the final size L^* of the system should be proportional to animal size L_a. Similarly, blastema size at the beginning of regeneration increases with animal size (Fig. 1C). Hence, in a simplified scenario, we also assume that the initial system size L_0 is proportional to L_a. To investigate how scaling of morphogen parameters could affect tissue growth, we investigate different scenarios for the size dependence of morphogen parameters.
We say that a morphogen gradient scales with a size ℓ if at least one of its features, source width w or pattern length-scale λ, both of which affect the signaling range, scales with this size ℓ. We distinguish two fundamentally different scaling scenarios, which differ by different interpretations of ℓ:

- *dynamic scaling* with growing blastema size $L(t)$, corresponding to the choice $\ell = L(t)$, and
- *static scaling with animal size* L_a, i.e. $\ell = L_a$.

For each of these two main scenarios, we consider three sub-scenarios. In all three sub-scenarios, we assume that the source region width and its position scale as $w \sim \ell$ and $x_0 \sim \ell$. In the first sub-scenario, which we term *source scaling*, the pattern length-scale λ is independent of size, see Fig. 3, left columns. In two additional sub-scenarios, in addition to source width, also the pattern length-scale scales as $\lambda \sim \ell$. According to Eq. 2, either the effective diffusion coefficient D or the morphogen degradation rate β must change with ℓ. This defines a second and third sub-scenario, which we refer to as D*-scaling* (i.e., $D \sim \ell^2$), and β*-scaling* ($\beta \sim \ell^{-2}$), respectively, see Fig. 3, middle

and right columns. The three sub-scenarios affect gradient amplitude A in different ways (SI appendix, Table S2): A increases with increasing size ℓ for source scaling, and even more so for β-scaling, where in addition to scaling of the source also the degradation rate β decreases for larger ℓ. In the case of D-scaling, the amplitude A stays approximately constant, as the effects of the scaling source and of the increase in D cancel.

Dynamic scaling with blastema size. In the absence of scaling, both the one-morphogen and the two-morphogen growth rules enable growth arrest. If the morphogen gradients exhibit dynamic scaling, model parameters and thus morphogen concentrations change dynamically with the growing blastema size $L(t)$. For most scenarios of dynamic scaling, concentrations stay approximately constant or even increase, and hence growth does not arrest anymore, see Fig. 3A. The only exception is growth arrest for the special case that the pattern length-scale λ does not scale, and the two-morphogen rule is assumed. We obtain similar results without scaling of the source (SI appendix, Table S2). Additionally, if either size w and position x_0 of the morphogen source scale, we obtain a combinatorial set of 32 sub-scenarios: growth arrests in 10 of these sub-scenarios for the two-morphogen growth rule, but only 4 sub-scenarios for the one-morphogen growth rule (SI appendix, Figs. S6 and S7). However, even if growth arrests, the final system size L^* is independent of the initial system size L_0. Thus, in the case of dynamic scaling with growing blastema size, proportional growth is not possible.

Scaling with animal size. Next, we explore the scenario of scaling with animal size, where the parameters of the morphogen dynamics are set by the animal size L_a and then remain constant during blastema growth. This could occur if those parameters are set by systemic factors (e.g. hormonal or metabolic). As parameters of the morphogen dynamics remain constant during blastema growth, for animals of fixed size, the system behaves exactly the same way as in the case without scaling. We conclude that growth will arrest under minimal assumptions as described in Fig. 2. However, the final blastema size L^* now depends on the animal size L_a in a non-trivial manner, see Fig. 3D. Proportional growth with $L^* \sim L_a$ is obtained exactly for D-scaling. For β-scaling, L^* increases super-linearly with L_a. These predictions are robust, and we obtain similar results, e.g. in the limit case of a point source (SI appendix, Table S2).

Combination of dynamic and static scaling. While Fig. 3C shows that dynamic scaling alone cannot ensure proportional growth, intriguingly, a combination of dynamic and static scaling can. For example, a scenario where all SHH parameters exhibit dynamic scaling and all FGF parameters exhibit static scaling ensures approximately proportional growth over a five-fold range of initial system sizes if D-scaling (i.e., size-dependent regulation of effective diffusion coefficients) is assumed (SI appendix, Fig. S8). This remains true even if all morphogen parameters – except FGF source size – exhibit dynamic scaling.

Quantification of size-dependent morphogen gradients

To assess putative scaling of morphogen gradients in regenerating axolotl limb blastema, we quantitatively analyzed SHH and FGF8 source regions in 3D in animals of different sizes and at several different regeneration time points. We used Hybridization Chain Reaction (HCR) RNA *in situ*, combined with tissue clearing and confocal microscopy to perform 3D quantitative measurements of SHH and FGF8 gradient parameters in developing limb buds and in regenerating limb blastemas from animals of three different sizes (snout-to-tail animal size: 3 cm, 5 cm, 7 cm). Measurements were taken at multiple time points (days post amputation, dpa) throughout the period when both signaling centers were present. We first quantified blastema size along the line in 3D passing through SHH and FGF8 source region centers, see Fig. 1C. Next, we quantified the linear sizes of SHH and FGF8 source regions by computing the cubic root of the volume enclosed by the 50%-iso-surfaces of the respective mRNA signals, which defines a length-scale that characterizes source size, see Fig. 4. We also quantified the gap size between the source regions and the tissue boundary corresponding to the source position x_0. Finally, the spatial range of FGF8 signaling was inferred from the volume enclosed by the 50%-iso-surface of *Dusp6* mRNA, a well-established downstream target of FGF8 signaling (Molina et al., 2007; Li et al., 2007; Ekerot et al., 2008). All morphogen gradient parameters exhibit a clear size dependence as a function of blastema size. To assess dynamic versus static scaling, we tested both a linear regression as a function of blastema size (left column in Fig 4B), and a linear regression as a function of animal size (right column). For both fit scenarios, we obtained satisfactory fits, with statistically significant size dependence, suggesting that both static and dynamic scaling may contribute to the observed size-dependent patterns. A contribution of dynamic scaling is suggested by the temporal increase of gradient parameters within some animal size groups (for separate linear regressions, see SI appendix, Fig. S9). On the other hand, static scaling with animal size is compatible with the data, with R^2 values only slightly smaller than those of the linear regression against blastema size. To gain further insight, we performed a partial correlation analysis on this data, which allows testing for conditional statistical independence (SI appendix, Table S3): After factoring out the influence of animal size, only 2% of the remaining variance of FGF8 source width w could be explained by blastema size, with a non-statistically significant correlation. In contrast, an analogous analysis for SHH source size revealed a

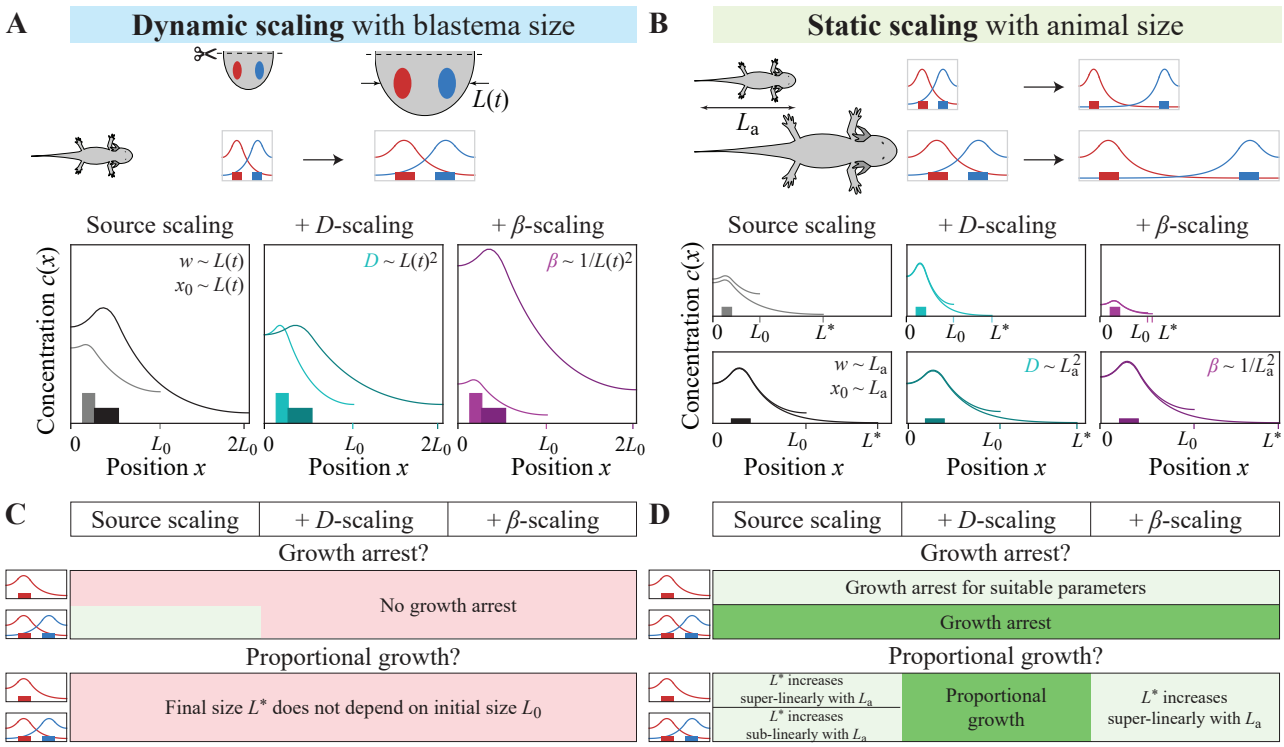

Figure 3. *Two scenarios of morphogen gradient scaling.* *A.* Schematic of *dynamic scaling*: morphogen gradients scale with growing blastema size $L(t)$. Different sub-scenarios of dynamic scaling affect the amplitude of morphogen gradients differently (source scaling with production rate $\alpha \sim L(t)$: black, D-scaling with effective diffusion coefficient $D \sim L(t)^2$: cyan, β-scaling with degradation rate $\beta \sim 1/L(t)^2$: magenta), see text for details. For each sub-scenario, source regions (boxes) and morphogen profiles (solid lines) are shown for initial tissue size L_0 and when tissue size has doubled in lighter and darker color, respectively. *B.* Schematic of *static scaling* with animal size: parameters of morphogen dynamics depend on animal size, but remain constant during growth. Same sub-scenarios of scaling as in panel A, but parameters of morphogen dynamics now depend on animal size L_a. Shown are morphogen gradients at the beginning of growth with initial system size L_0 (assumed proportional to L_a for simplicity) and at growth arrest with final system size L^* for two values of L_0 (upper and lower row). *C.* Summary of modeling predictions for *dynamic scaling* with blastema size, corresponding to the three scaling sub-scenarios introduced in panel A. For *dynamics scaling*, growth arrests for any growth threshold Θ for the two-morphogen growth rule if the morphogen source scales, but not the pattern length-scale λ, but not for any other sub-scenario. However, even in the scenario with growth arrest, the final system size L^* is independent of initial system size, i.e. there is no proportional growth. *D.* Summary of modeling predictions for *static scaling* with animal size, corresponding to the three scaling sub-scenarios introduced in panel B. For static scaling, morphogen dynamics parameters remain constant during growth. Correspondingly, growth arrests for any growth threshold Θ for the two-morphogen growth rule (introduced in Fig. 2), yet for the one-morphogen rule only if the growth threshold Θ exceeds a critical value Θ_c. Proportional growth is achieved for the D-scaling sub-scenario, where both the effective diffusion coefficient D and the source region scales with animal size.

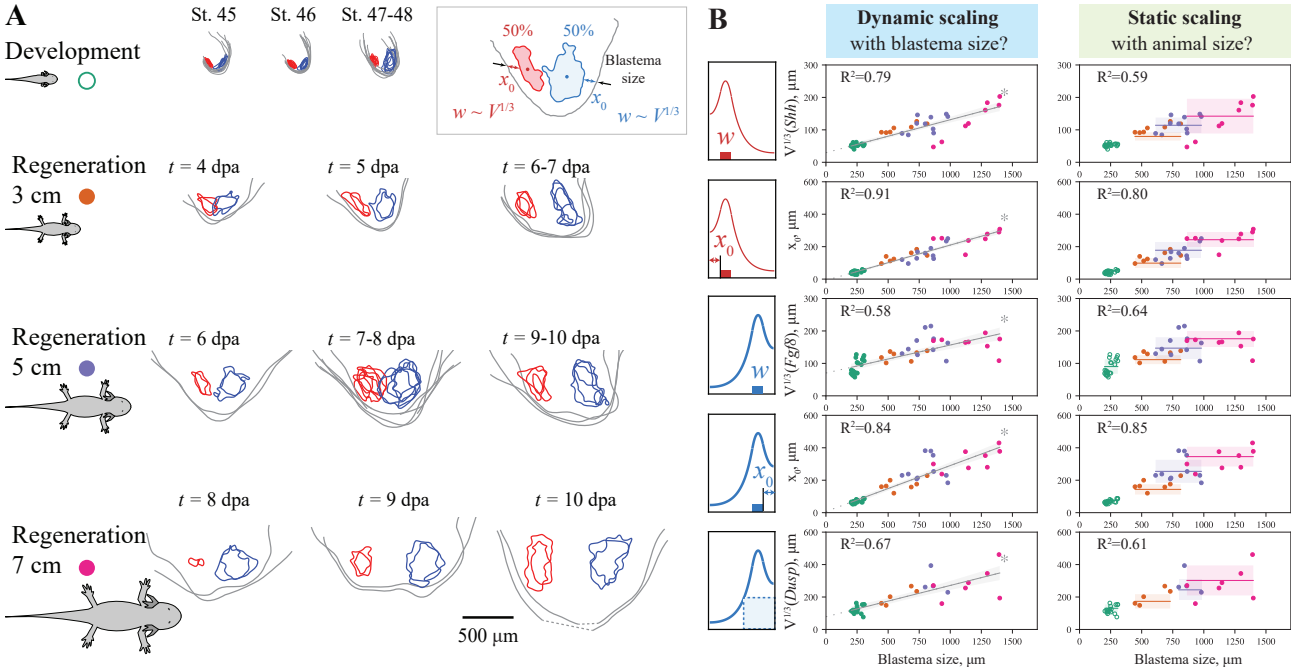

Figure 4. *Size-dependence of SHH and FGF8 morphogen gradients. A.* Outlines of SHH and FGF8 source regions from *in situ* hybridization in regenerating blastemas of different-sized animals at different developmental stages and at different regeneration time points (registered overlays of all samples; *Shh*: red, *Fgf8*: blue, 50% threshold of normalized intensity, shown as binary projections along dorsal-ventral axis on plane containing the centers of the *Shh* and *Fgf8* regions, see SI appendix for details). *B.* Quantification of morphogen gradient parameters as function of limb bud or blastema size (from top to bottom): linear source size $V^{1/3}$ determined from 3D-volume V enclosed by 50%-iso-surface for *Shh* corresponding to source width w, same for *Fgf8*; gap size between SHH source boundary and tissue boundary corresponding to the source position x_0 (measured in 2D-projections along a line connecting the centers of the *Shh* and *Fgf8* regions as shown in panel A), same for FGF8; proxy for FGF8 signaling range determined as $V^{1/3}$ from the 3D-volume V enclosed by the 50%-iso-surface of the FGF8 target *Dusp6*. Left and right columns show the same data with different fits for each morphogen gradient parameter: linear regression as function of blastema size (left, corresponding to *dynamic scaling* with blastema size), constant fit with constants that depend linearly on animal size (right, *static scaling* with animal size). Colors represent animal size as in panel A and Fig. 1C (filled circles: regeneration, open green circles: development).

much higher explained variance of 59% with high significance levels $p < 0.1\%$, indicative of a contribution of dynamic scaling for SHH. The statistical analysis for the other morphogen parameters suggests different contributions of static and dynamic scaling, see SI appendix. In conclusion, the data for the FGF8 source region and possibly other morphogen gradient parameters is compatible with static scaling. Note that in our model, it is sufficient if only a subset of morphogen parameters, e.g. only FGF8 source size, exhibit static but not dynamic scaling, to ensure growth arrest and proportional growth (SI appendix, Fig. S8).

Mutual feedback between morphogens

Previous works suggested a mutual feedback between SHH and FGF production (Laufer et al., 1994; Niswander et al., 1994; Bénazet et al., 2009). Above, we assumed that both morphogens are produced independently of each other and their source regions and production rates remain constant during tissue growth without specifying biological mechanisms of maintaining morphogen production. Here, we theoretically describe a possible minimal feedback scenario. We assume that there are regions competent for SHH or FGF8 production (shown as transparent regions in Fig. 5A). This assumption is supported by distinct properties of anterior and posterior blastema regions (Otsuki et al., 2023; Carlson, 1975; Endo et al., 2004; Bryant, 1976). We further assume that SHH and FGF8 are produced in their respective competent region if the opposite morphogen concentration is above a feedback threshold $\Theta_{\rm fb}$. With such mutual feedback, the system can be in one of two limiting regimes, depending on the relative magnitude of the growth threshold Θ and the feedback threshold $\Theta_{\rm fb}$. In the first regime, growth arrests because the growth threshold is reached first (green region in Fig. 5B). The system thus behaves similar to the case without feedback described above and arrests growth, while morphogen production in still ON. In the second regime, the feedback threshold is reached first (orange region in Fig. 5B). As a consequence, the source regions of morphogen production shrink rapidly, and morphogen production is switched OFF. Without morphogen production, also tissue growth arrests.

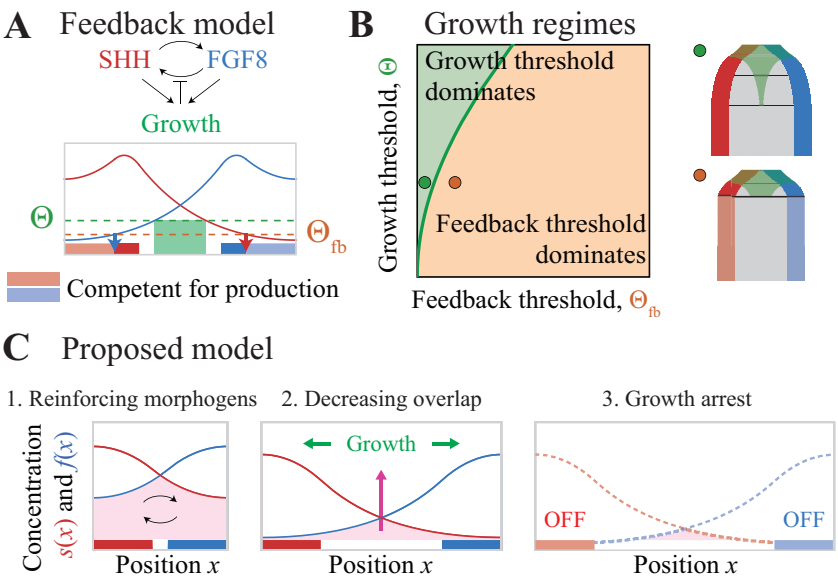

Figure 5. *Feedback model of reinforcing morphogens.* *A.* Minimal model of mutual feedback between oppositely-oriented morphogen gradients: Each morphogen can only be produced in a region of competent cells (transparent red and blue bars) where the concentration of the respective other morphogen exceeds a threshold (Θ_{fb}, orange dashed), defining two source regions (solid red and blue bars). *B.* Phase diagram of growth regimes as a function of growth threshold Θ and feedback threshold Θ_{fb}, here shown for the two-morphogen growth rule, exhibiting two regimes: the growth threshold Θ dominates, resulting in dynamics analogous to the case without feedback (green) as in Fig. 2, or, the feedback threshold Θ_{fb} dominates, resulting in instantaneous and homogeneous growth arrest across the entire system (orange). *C.* Model of growth arrest by the growth-threshold regime: 1. The tissue grows (green) where both morphogens (red and blue) are above the growth threshold (green dashed). 2. Tissue growth pushes the two morphogen sources apart, thus decreasing the region where the two morphogens overlap. 3. Due to the mutual feedback between the two morphogens, their respective source regions start shrinking rapidly, switching off both morphogens and arresting growth.

In this second regime, the feedback between the two morphogens functions as a tissue-level ON/OFF switch for growth. While Fig. 5B shows results for the two-morphogen growth rule, the system behaves qualitatively similarly for the one-morphogen growth rule. Signaling delays of morphogen feedback would result in a gradual decrease of morphogen profile amplitudes, but otherwise similar behavior.

Adding feedback to the system thus does not significantly change its behavior with regard to growth arrest, demonstrating that our conclusions remain applicable also in a more realistic model. Feedback between the two morphogens could be a means of avoiding the slow fade-out of growth observed without feedback (Fig. 2), or even of switching off growth homogeneously throughout the system.

Discussion

Inspired by the size-adaptive regeneration of axolotl limbs, we addressed the general question of how morphogen-dependent tissue growth can be arrested once a tissue has reached its correct size. In our prototypical minimal model, tissue growth is induced by a threshold rule for either a single morphogen, or a pair of oppositely-oriented morphogen gradients. The two-morphogen growth rule with two oppositely-oriented gradients provides a particularly robust mechanism of growth arrest: the overlap between the two gradients induces growth; this growth increases the spatial separation between the two morphogen sources and thus decreases the overlap between the two gradients. This negative feedback loop robustly terminates growth at a specific tissue size. Proportional growth, however, where the final system size is proportional to initial size, requires scaling of morphogen gradients. We distinguished two fundamental scaling scenarios: *dynamic scaling* of morphogen gradients with the growing blastema, or *static scaling*, where morphogen gradient parameters depend on animal size, but remain constant during growth. Our theoretical analysis shows that static scaling with animal size of at least a subset of morphogen parameters is necessary and sufficient for proportional growth if a switch-like growth rule is assumed (Fig. 3 and Fig. S8 in SI appendix). We expect similar results for graded growth responses.

Blastema growth in axolotl regeneration is more complex. Our analysis addresses only the first stage of blastema outgrowth, which is followed by cell differentiation and a second growth phase. The second phase, which is independent of SHH-FGF signaling, is thought to be regulated by neuronal signals (Wells et al., 2021). Nevertheless,

the first growth phase and the blastema size at the onset of tissue differentiation is important to ensure accurate limb patterning, including the correct number of bone elements. Interestingly, blastema growth is not proportional to limb size in very large animals ($\gtrsim$ 10 cm) and is more accurately described by allometric scaling laws (Furukawa et al., 2024) (confirmed also in SI appendix, Fig. S1). This suggests limits of scaling. While we focused on proportional growth, it is interesting to note that certain sub-scenarios considered (e.g., source scaling with animal size, assuming a one-morphogen growth rule), predict a sublinear dependence of final system size on animal size, similar to experimental observations in large axolotls. While our minimal model showed that exclusively dynamic scaling cannot enable proportional growth, it is likely that a combination of dynamic and static scaling applies in axolotl. Furthermore, dynamic scaling could still be compatible with proportional blastema growth if a separate timer mechanism terminates growth after a fixed time.

We used *in situ* hybridization in 3D tissues to quantify SHH and FGF8 source regions and FGF8 signaling range in developing limb buds and regenerating blastemas of different sizes at different time points. We find a clear size-dependence of morphogen gradient parameters. In particular, our data suggests static scaling with animal size for the FGF8 source region size, while the SHH source region size may exhibit dynamic scaling. This extends the recently published *in situ* hybridization analysis of source sizes in tissue slices for a single morphological stage in (Furukawa et al., 2024). Our analysis of growth control by scaling morphogen gradients is independent of the particular implementation of morphogen scaling, and only depends on which parameters of morphogen dynamics are adjusted in a size-dependent manner. Scaling of morphogen gradients has been reported in a number of systems (Ben-Zvi et al., 2011; Wartlick et al., 2011b; Stückemann et al., 2017; Mateus et al., 2020; Romanova-Michaelides et al., 2022; Kicheva and Briscoe, 2023; Nikolić et al., 2024). A common concept in proposed mechanisms is the presence of a modulator such as an “expander”, whose concentration regulates, e.g., the effective diffusion coefficient or degradation rate of a morphogen (Ben-Zvi and Barkai, 2010; Werner et al., 2015; Umulis and Othmer, 2013; Shilo and Barkai, 2017). In expander-dilution models, tissue growth dilutes the concentration of the expander inversely proportional to tissue volume (Wartlick et al., 2011a). In expander-repression models, the production of the expander depends on the morphogen itself (Ben-Zvi and Barkai, 2010). Recently, SCUBE family molecules were shown to affect SHH spreading (Schlissel et al., 2024) and suggested to act by an expansion-repression mechanism to control the amplitude and pattern length-scale of the SHH gradient in the zebrafish neural tube (Collins et al., 2018), compatible with a mechanism of D-scaling.

SHH and FGF8 also guide limb development in other vertebrates (Muneoka and Bryant, 1982; Payzin-Dogru and Whited, 2018). This pair of morphogen gradients must be switched on, but later also switched off again. Previous mathematical models focused on the temporal dynamics of morphogens (Bénazet et al., 2009), including the role of intermediate morphogens Bone Morphogenetic Protein (BMP) and Gremlin (GREM), which itself are thought to be a part of the SHH-FGF feedback loop. To explain how SHH and FGF become switched off again, various hypotheses reviewed in (Zuniga and Zeller, 2020) were put forward: A first hypothesis suggests that the medial portion of the SHH competent region, which previously expressed SHH, loses this competence, creating an expanding region of cells that are not competent to express either SHH or GREM or FGF8 (Scherz et al., 2004). A second hypothesis suggests that FGF8 terminates GREM in a concentration-dependent manner (Verheyden and Sun, 2008); alternatively, a low concentration of BMP could activate GREM at early stages, while a higher concentration of BMP could suppress GREM later (Nissim et al., 2006). We comment that these hypotheses would require signal delays to prevent becoming trapped in an intermediate state between “on” and “off”. Another hypothesis would be a timer mechanism that switches off SHH and FGF after a preset growth period (Saiz-Lopez et al., 2015). These hypotheses not only underline the intricate molecular interactions involved in the growth control of developing and regenerating limbs but also start to appreciate the importance of spatial patterns of signaling.

Our model proposes that a coupling of spatial patterns and growth provides a simple and robust mechanism by which the SHH-FGF feedback loop could become switched off after the first stage of blastema outgrowth is completed (Fig. 5C). Our minimal model suggests specific experiments. Quantifying SHH and FGF8 morphogen gradients as function of animal size and time, ideally by measuring protein concentrations instead of down-stream signaling, will allow testing our theory prediction of static scaling with animal size (or limb size). Cell culture experiments with controlled levels of morphogens as initiated in (Furukawa et al., 2024) could test the growth rules proposed here. This could pave the road towards more realistic, data-driven models that capitalize on the concepts laid out in the idealized, one-dimensional model studied here. In conclusion, we proposed a simple mechanism of two opposing morphogen gradients that reinforce each other, to enable robust growth arrest and proportional tissue growth by scaling of morphogen parameters with animal size.

Methods

Numerical methods

In the presence of tissue growth with local growth rate $g(x,t)$, Eq. (1) changes to

$$\partial_t c(x,t) = D\,\partial_x^2 c - \partial_x[v(x,t)c] - [\beta + g(x,t)]c + \alpha\,\chi_{w(t)}(x) \quad , \tag{4}$$

where $\partial_x v = g$. This equation is numerically solved using a modified Euler scheme in a Lagrangian frame with non-uniform spatial grid, whose bin sizes Δx_i are updated according to $\Delta x_i(t_n+1) = [1+g(x_i,t_n)\Delta t]\Delta x_i(t_n)$.

Whole-mount HCR *in situ* hybridization and imaging

Shh, *Fgf8* and *Dusp6* mRNAs were detected in formaldehyde-fixed limb blastema and developing limb buds obtained from different-sized animals at different timepoints by whole mount HCR, a fluorescent RNA *in situ* method as described in (Choi et al., 2018) with minor modifications, followed by refractive index matching and confocal imaging in 3D (for detailed protocol, see SI appendix).

Image analysis

For analysis of 3D multi-channel z-stack images, blastemas were segmented using APOC (Haase et al., 2023) trained with user-specified ground truth labels applied to the *Shh* channel using Napari (Chiu et al., 2022) and custom Python code. Blood vessels detected in the autofluorescence channel were segmented using APOC, and the corresponding binary mask was excluded from all channels. The linear size of SHH and FGF8 source regions, as well as of FGF8 signaling indicated by *Dusp6* mRNA, were determined as the cubic roots of the volumes enclosed by the respective 50%-iso-intensity surfaces (after denoising and min-max normalization of each channel). Blastema size was measured in 3D images along a line passing through the centers of the *Shh* and *Fgf8* regions. Gap sizes between the blastema boundary and the boundaries of these source regions (x_0) were measured along the same line, yet using 2D-projections to account for a possible non-convex shape of source regions.

Acknowledgements.

We thank Leo Otsuki and Elly M. Tanaka (IMBA) for the transgenic axolotl line (tgSceI(ZRS:TFPnls-T2A-ERT2-Cre-ERT2)^{Etnka}. We thank Elly M. Tanaka, as well as all members of the Sandoval-Guzmán and Friedrich groups for stimulating discussions, the animal carers of the CRTD (Beate Gruhl and Anja Wagner) for dedicated axolotl care, the light microscopy facility of the CMCB for excellent support, as well as Veikko F. Geyer and Maximilian Kotz for statistical analysis support. TSG and BMF acknowledge funding from a joint D-A-CH grant from the German and Austrian Science Foundations (441649267, jointly with Elly M. Tanaka). BMF was additionally supported by the Deutsche Forschungsgemeinschaft (DFG, German Research Foundation) under Germany's Excellence Strategy - EXC-2068-390729961, as well as through a Heisenberg grant (421143374).

References

Ben-Zvi, D. and Barkai, N. (2010). Scaling of morphogen gradients by an expansion-repression integral feedback control. *Proceedings of the National Academy of Sciences*, 107(15):6924–6929.

Ben-Zvi, D., Pyrowolakis, G., Barkai, N., and Shilo, B.-Z. (2011). Expansion-repression mechanism for scaling the dpp activation gradient in drosophila wing imaginal discs. *Current biology*, 21(16):1391–1396.

Bénazet, J.-D., Bischofberger, M., Tiecke, E., Gonçalves, A., Martin, J. F., Zuniga, A., Naef, F., and Zeller, R. (2009). A self-regulatory system of interlinked signaling feedback loops controls mouse limb patterning. *Science*, 323(5917):1050–1053.

Bryant, S. V. (1976). Regenerative failure of double half limbs in notophthalmus viridescens. *Nature*, 263(5579):676–679.

Carlson, B. M. (1975). The effects of rotation and positional change of stump tissues upon morphogenesis of the regenerating axolotl limb. *Developmental Biology*, 47(2):269–291.

Chiu, C.-L., Clack, N., et al. (2022). Napari: a python multi-dimensional image viewer platform for the research community. *Microscopy and Microanalysis*, 28(S1):1576–1577.

Choi, H. M., Schwarzkopf, M., Fornace, M. E., Acharya, A., Artavanis, G., Stegmaier, J., Cunha, A., and Pierce, N. A. (2018). Third-generation in situ hybridization chain reaction: multiplexed, quantitative, sensitive, versatile, robust. *Development*, 145 (12):dev165753.

Collins, Z. M., Ishimatsu, K., Tsai, T. Y., and Megason, S. G. (2018). A scube2-shh feedback loop links morphogen release to morphogen signaling to enable scale invariant patterning of the ventral neural tube. *BioRxiv*, page 469239.

Dinsmore, C. E. (2004). Urodele limb and tail regeneration in early biological thought: an essay on scientific controversy and social change. *International Journal of Developmental Biology*, 40(4):621–627.

Ekerot, M., Stavridis, M. P., Delavaine, L., Mitchell, M. P., Staples, C., Owens, D. M., Keenan, I. D., Dickinson, R. J., Storey, K. G., and Keyse, S. M. (2008). Negative-feedback regulation of fgf signalling by dusp6/mkp-3 is driven by erk1/2 and mediated by ets factor binding to a conserved site within the dusp6/mkp-3 gene promoter. *Biochemical Journal*, 412(2):287–298.

Endo, T., Bryant, S. V., and Gardiner, D. M. (2004). A stepwise model system for limb regeneration. *Developmental biology*, 270 (1):135–145.

Furukawa, S., Yamamoto, S., Ohashi, A., Morishita, Y., and Satoh, A. (2024). Allometry in limb regeneration and scale-invariant patterning as the basis of normal morphogenesis from different sizes of blastemas. *Development*, pages dev–202697.

Glotzer, G. L., Tardivo, P., and Tanaka, E. M. (2022). Canonical wnt signaling and the regulation of divergent mesenchymal fgf8 expression in axolotl limb development and regeneration. *Elife*, 11:e79762.

Haase, R., Lee, D., Pop, D. D., and Žigutytė, L. (2023). haesleinhuepf/napari-accelerated-pixel-and-object-classification: 0.14. 1. *Zenodo https://doi. org/10.5281/zenodo*, 10071078.

Han, M.-J., An, J.-Y., and Kim, W.-S. (2001). Expression patterns of fgf-8 during development and limb regeneration of the axolotl. *Developmental Dynamics*, 220(1):40–48.

Kicheva, A. and Briscoe, J. (2023). Control of tissue development by morphogens. *Annual review of cell and developmental biology*, 39(1):91–121.

Laufer, E., Nelson, C. E., Johnson, R. L., Morgan, B. A., and Tabin, C. (1994). Sonic hedgehog and fgf-4 act through a signaling cascade and feedback loop to integrate growth and patterning of the developing limb bud. *Cell*, 79(6):993–1003.

Leigh, N. D. and Currie, J. D. (2022). Rebuilding limbs, one cell at a time. *Developmental Dynamics*, 251(9):1389.

Li, C., Scott, D. A., Hatch, E., Tian, X., and Mansour, S. L. (2007). Dusp6 (mkp3) is a negative feedback regulator of fgf-stimulated erk signaling during mouse development. *Development*, 134(1):167–176.

Mateus, R., Holtzer, L., Seum, C., Hadjivasiliou, Z., Dubois, M., Jülicher, F., and Gonzalez-Gaitan, M. (2020). Bmp signaling gradient scaling in the zebrafish pectoral fin. *Cell reports*, 30(12):4292–4302.

Molina, G. A., Watkins, S. C., and Tsang, M. (2007). Generation of fgf reporter transgenic zebrafish and their utility in chemical screens. *BMC developmental biology*, 7:1–14.

Muneoka, K. and Bryant, S. V. (1982). Evidence that patterning mechanisms in developing and regenerating limbs are the same. *Nature*, 298(5872):369–371.

Nacu, E., Gromberg, E., Oliveira, C. R., Drechsel, D., and Tanaka, E. M. (2016). FGF8 and SHH substitute for anterior–posterior tissue interactions to induce limb regeneration. *Nature*, 533(7603):407–410.

Nikolić, M., Antonetti, V., Liu, F., Muhaxheri, G., Petkova, M. D., Scheeler, M., Smith, E. M., Bialek, W., and Gregor, T. (2024). Scale invariance in early embryonic development. *Proceedings of the National Academy of Sciences*, 121(46):e2403265121.

Nissim, S., Hasso, S. M., Fallon, J. F., and Tabin, C. J. (2006). Regulation of gremlin expression in the posterior limb bud. *Developmental biology*, 299(1):12–21.

Niswander, L., Jeffrey, S., Martin, G. R., and Tickle, C. (1994). A positive feedback loop coordinates growth and patterning in the vertebrate limb. *Nature*, 371(6498):609–612.

Otsuki, L., Plattner, S. A., Taniguchi-Sugiura, Y., and Tanaka, E. M. (2023). Molecular basis for positional memory and its reprogrammability in limb regeneration. *bioRxiv*, pages 2023–10.

Payzin-Dogru, D. and Whited, J. L. (2018). An integrative framework for salamander and mouse limb regeneration. *The International journal of developmental biology*, 62(6-7-8):393–402.

Purushothaman, S., Elewa, A., and Seifert, A. W. (2019). Fgf-signaling is compartmentalized within the mesenchyme and controls proliferation during salamander limb development. *Elife*, 8:e48507.

Romanova-Michaelides, M., Hadjivasiliou, Z., Aguilar-Hidalgo, D., Basagiannis, D., Seum, C., Dubois, M., Jülicher, F., and Gonzalez-Gaitan, M. (2022). Morphogen gradient scaling by recycling of intracellular dpp. *Nature*, 602(7896):287–293.

Saiz-Lopez, P., Chinnaiya, K., Campa, V. M., Delgado, I., Ros, M. A., and Towers, M. (2015). An intrinsic timer specifies distal structures of the vertebrate limb. *Nature communications*, 6(1):8108.

Scherz, P. J., Harfe, B. D., McMahon, A. P., and Tabin, C. J. (2004). The limb bud shh-fgf feedback loop is terminated by expansion of former zpa cells. *Science*, 305(5682):396–399.

Schlissel, G., Meziane, M., Narducci, D., Hansen, A. S., and Li, P. (2024). Diffusion barriers imposed by tissue topology shape hedgehog morphogen gradients. *Proceedings of the National Academy of Sciences*, 121(36):e2400677121.

Shilo, B.-Z. and Barkai, N. (2017). Buffering global variability of morphogen gradients. *Developmental cell*, 40(5):429–438.

Stückemann, T., Cleland, J. P., Werner, S., Vu, H. T.-K., Bayersdorf, R., Liu, S.-Y., Friedrich, B., Jülicher, F., and Rink, J. C. (2017). Antagonistic self-organizing patterning systems control maintenance and regeneration of the anteroposterior axis in planarians. *Developmental cell*, 40(3):248–263.

Tickle, C. and Towers, M. (2017). Sonic hedgehog signaling in limb development. *Frontiers in cell and developmental biology*, 5: 14.

Torok, M. A., Gardiner, D. M., Izpisúa-Belmonte, J.-C., and Bryant, S. V. (1999). Sonic hedgehog (shh) expression in developing and regenerating axolotl limbs. *Journal of Experimental Zoology*, 284(2):197–206.

Umulis, D. M. and Othmer, H. G. (2013). Mechanisms of scaling in pattern formation. *Development*, 140(24):4830–4843.

Verheyden, J. M. and Sun, X. (2008). An fgf/gremlin inhibitory feedback loop triggers termination of limb bud outgrowth. *Nature*, 454(7204):638–641.

Vieira, W. A., Wells, K. M., and McCusker, C. D. (2020). Advancements to the axolotl model for regeneration and aging. *Gerontology*, 66(3):212–222.

Wartlick, O., Mumcu, P., Jülicher, F., and Gonzalez-Gaitan, M. (2011). Understanding morphogenetic growth control—lessons from flies. *Nature Reviews Molecular Cell Biology*, 12(9):594–604.

Wartlick, O., Mumcu, P., Kicheva, A., Bittig, T., Seum, C., Jülicher, F., and Gonzalez-Gaitan, M. (2011). Dynamics of dpp signaling and proliferation control. *science*, 331(6021):1154–1159.

Wells, K. M., Kelley, K., Baumel, M., Vieira, W. A., and McCusker, C. D. (2021). Neural control of growth and size in the axolotl limb regenerate. *Elife*, 10:e68584.

Werner, S., Stückemann, T., Beirán Amigo, M., Rink, J. C., Jülicher, F., and Friedrich, B. M. (2015). Scaling and regeneration of self-organized patterns. *Physical review letters*, 114(13):138101.

Wolpert, L. (1969). Positional information and the spatial pattern of cellular differentiation. *Journal of theoretical biology*, 25(1): 1–47.

Young, J. J. and Tabin, C. J. (2017). Saunders's framework for understanding limb development as a platform for investigating limb evolution. *Developmental biology*, 429(2):401–408.

Zuniga, A. and Zeller, R. (2020). Dynamic and self-regulatory interactions among gene regulatory networks control vertebrate limb bud morphogenesis. *Current topics in developmental biology*, 139:61–88.

Supporting Information for

Static morphogen scaling enables proportional growth in tissue growth model inspired by axolotl limb regeneration

Natalia Lyubaykina, Dunja Knapp, Pietro Tardivo, Tatiana Sandoval-Guzmán, Benjamin M. Friedrich

This PDF file includes:

1. Figures S1 to S9
2. Tables S1 to S3
3. Supplementary Note 1: Supplementary Methods
4. Supplementary Note 2: Supplementary Information for Mathematical Modeling

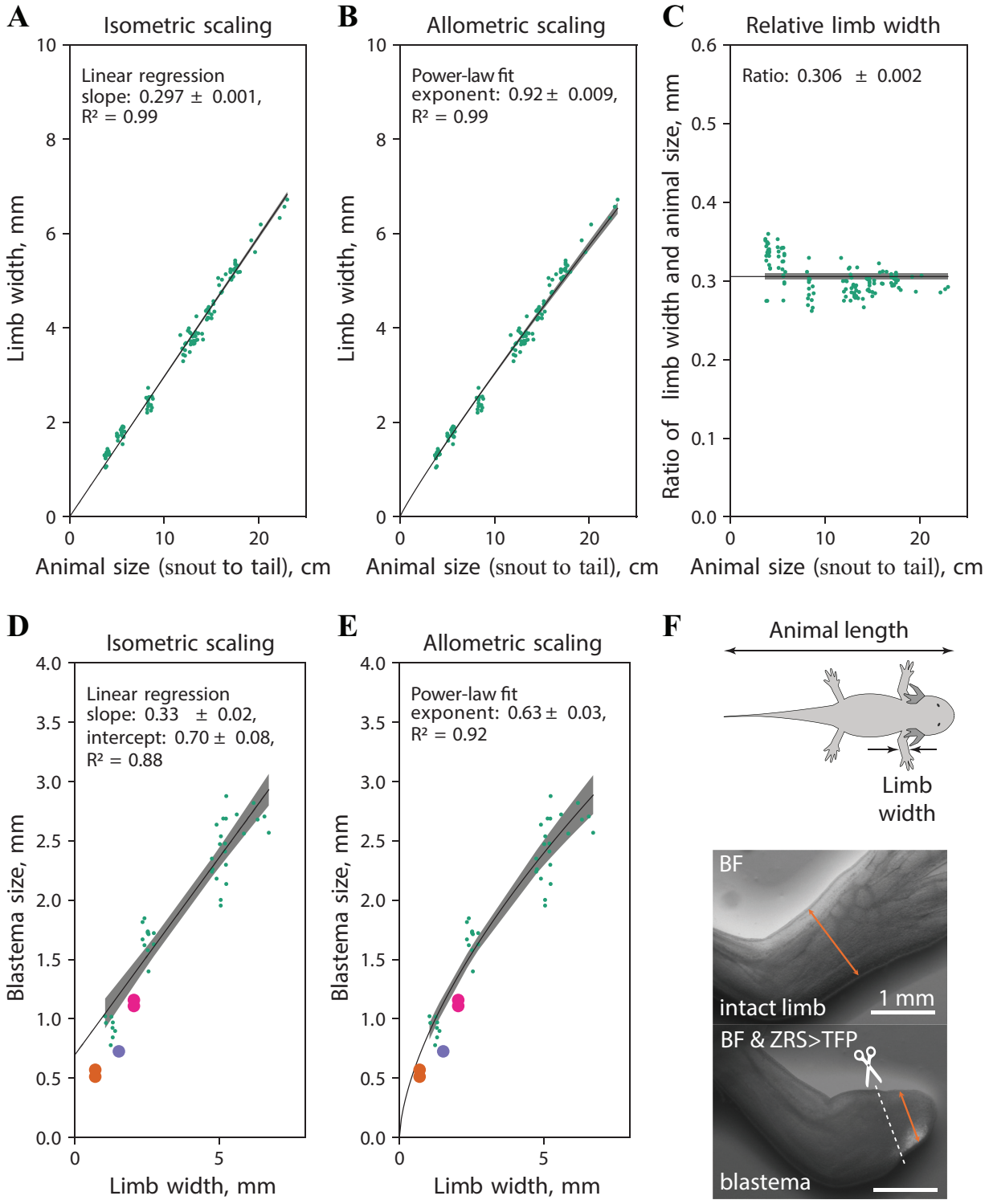

Figure S1. *Measurements of animal size, limb width, and characteristic blastema size.* *A.* Limb width as function of animal size, together with proportional fit (isometric scaling). *B.* Same data as in panel A, but with power-law fit of an allometric scaling relation. *C.* The relative limb width stays approximately constant as function of animal size. *D.* Characteristic blastema size (green dots, see Panel F and Methods in SI appendix for details of measurement) as function of limb width, together with proportional fit (isometric scaling). Note that blastema size appears to plateau for larger limb width (larger animals). For comparison, blastema size as shown in Fig. 1C measured along a line connecting the centers of SHH and FGF8 source regions is shown for 3-cm animal at 5 dpa (orange), 5-cm animal at 7 dpa (blue), 7-cm animal at 9 dpa (magenta), using the linear regression from panel S1A to relate animal size and limb width. *E.* Same data as in panel D, but with power-law fit of an allometric scaling relation. *F.* Schematic of limb and blastema size measurements from wide-field images; the orange line indicates the position of the limb/blastema size measurement. For the limb, the measurement plane is the same position as the amputation plane (white dotted line). For the blastema, the measurement plane goes through the center of the TFP>ZRS reporter expression, parallel to the amputation plane.

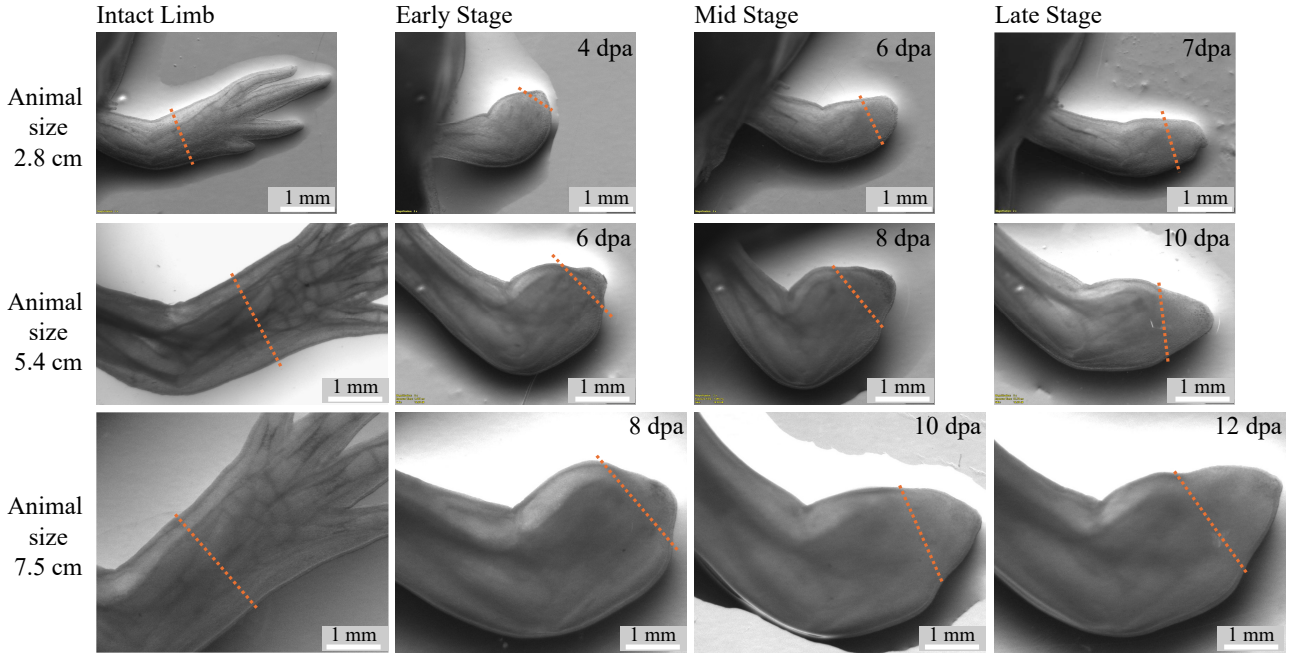

Figure S2. *Regeneration time-course in animals of three different sizes.* Intact limbs and three analogous stages of regeneration (early, middle and late blastema stages) are shown for animals of different sizes: 2.8 cm, 5.4 cm and 7.5 cm length from snout to tail. Analogous time points were designated based on morphology and FGF8 and SHH morphogen dynamics. The orange dotted lines indicate the amputation plane. Days post amputation (dpa) are indicated. Early stage: initial cohort of undifferentiated cells accumulated underneath the wound epidermis and onset of FGF8 and SHH expression, mid-stage: fast-growing blastema, FGF8 expressed in a single contiguous cloud, late stage: blastema began to flatten along the dorsoventral axis, FGF8 source region begins to split into dorsal and ventral cloud.

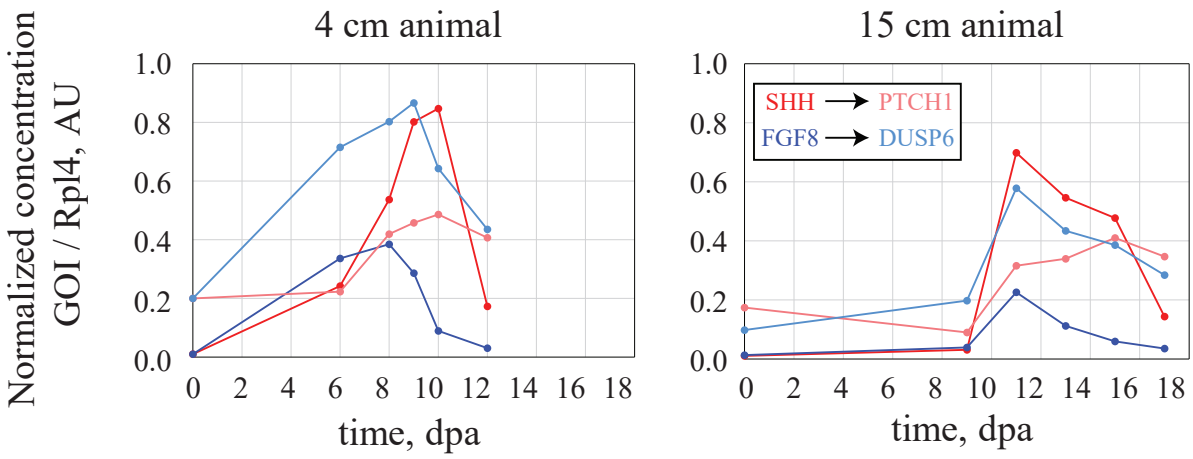

Figure S3. *Quantitative PCR analysis of Shh, Fgf8, and their downstream targets Ptch1 and Dusp6 during regeneration in animals of two different sizes.* Experimentally measured mRNA values for each Gene of Interest (GOI) were normalized to the housekeeping gene *Rpl4* and presented in arbitrary units. The data represent mean values from two independent experiments. The approximately equal amplitudes of normalized SHH and FGF8 expression, together with the size-scaling of source regions shown in Fig. 4B, is consistent with the assumption of a size-independent morphogen production rate constant (parameter α in the model).

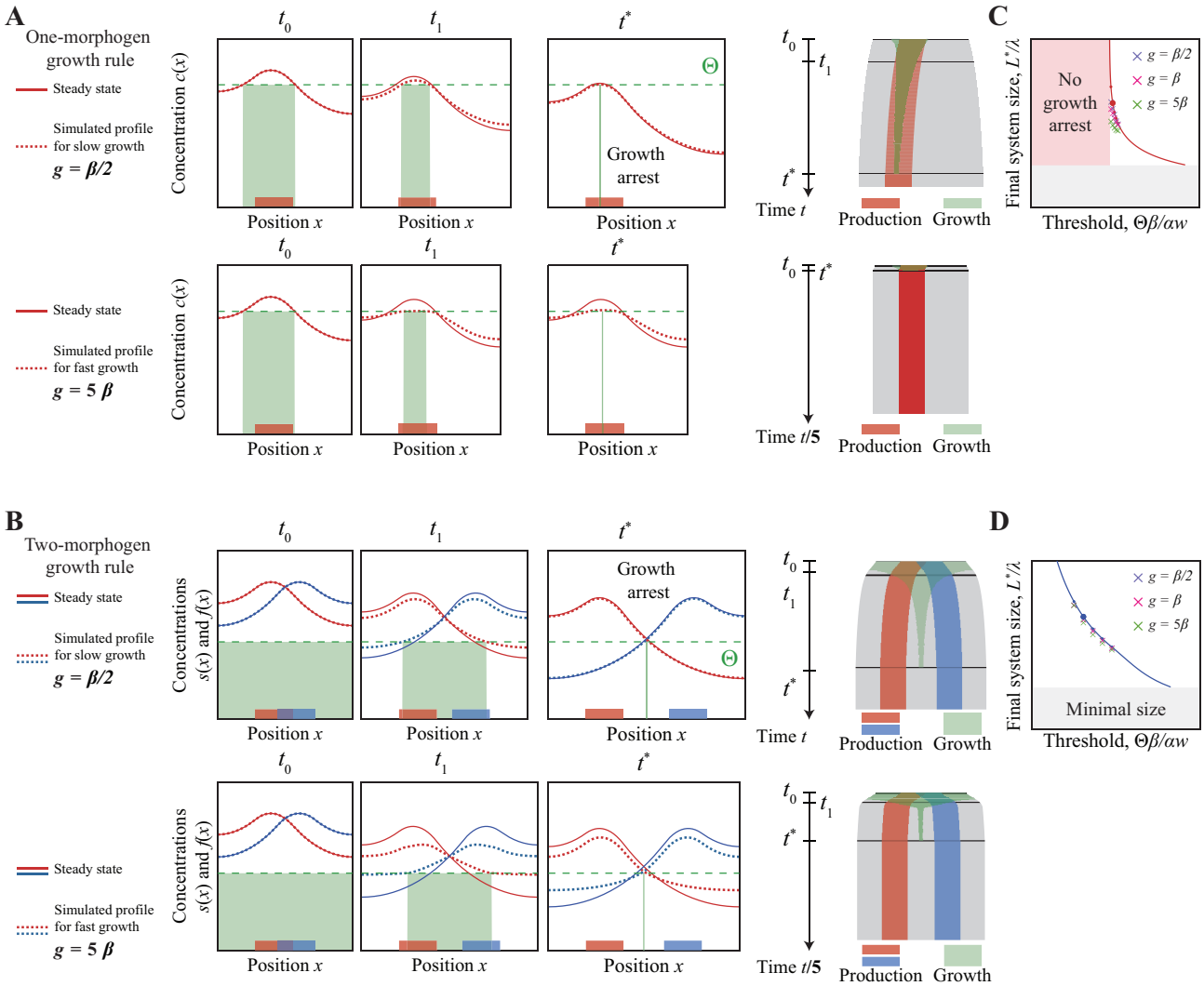

Figure S4. *Effect of finite growth rate.* *A.* Morphogen source region (red region), morphogen gradient (red curve), growth threshold Θ (dashed green line), and growth zone (green region) at different time points for the one-morphogen growth rule analogous to Fig. 2A, yet for finite growth rate g, resulting in non-steady-state concentration profiles. Dashed lines show morphogen profiles computed for the case of a finite growth rate g for two values of g (upper and lower panel, respectively), solid lines show morphogen profiles in the limit case of slow growth as considered in Fig. 2A. Corresponding kymographs of computed tissue growth analogous to Fig. 2A are shown to the right. *B.* Morphogen source region (red region), morphogen gradient (red curve), growth threshold Θ (dashed green line), and growth zone (green region) at different time points for the two-morphogen growth rule analogous to Fig. 2B, for a finite growth rate g. As in panel S4A, dashed lines show morphogen profiles computed for the case of a finite growth rate g for the values of g, solid lines show morphogen profiles in the limit case of slow growth as considered in Fig. 2B. Corresponding kymographs of computed tissue growth analogous to Fig. 2B are shown to the right. *C, D.* Final system size L^* normalized by pattern length-scale λ as function of a normalized growth threshold $\Theta\beta/\alpha w$ for the one-morphogen growth rule. Also shown are values of final system size for selected growth rates. Parameters: see Table S1, except growth thresholds for one-morphogen growth rule $\Theta = 0.25$, for two-morphogen growth rule $\Theta = 0.1379$, also shown in Panels C and D.

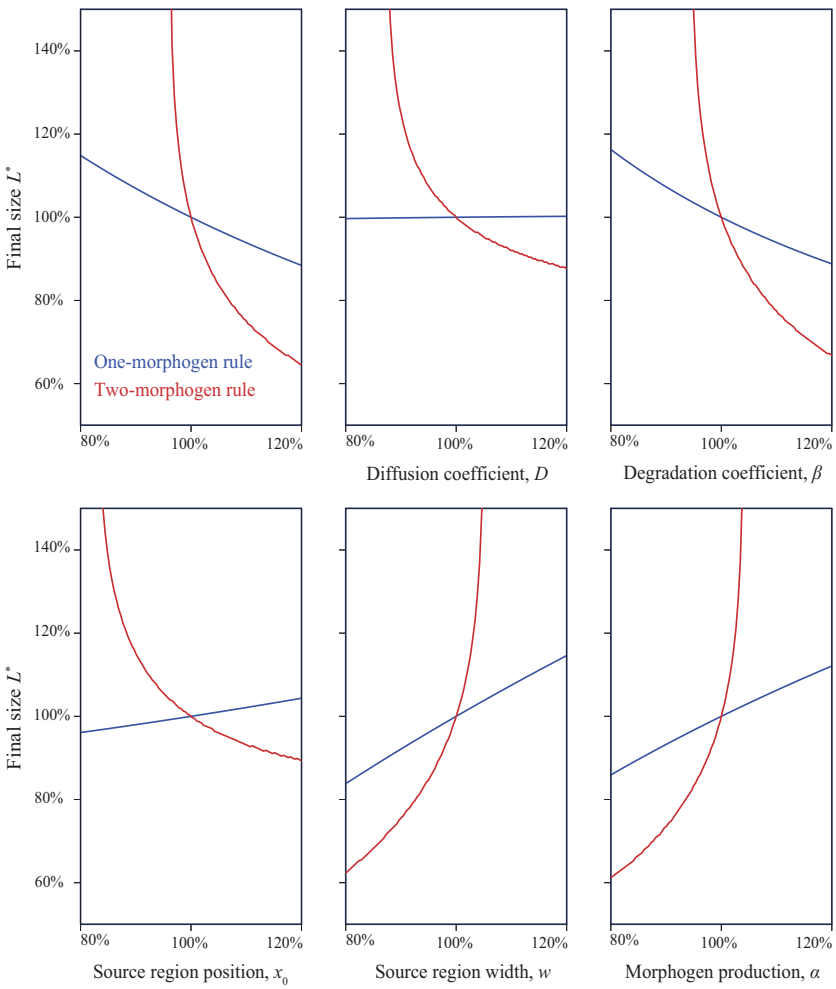

Figure S5. *Sensitivity of final system size to variations of model parameters.* Plots show the final system size L^* as function of all model parameters: growth threshold Θ, diffusion coefficient D, degradation coefficient β, source region position x_0 and its width w, production rate α. Red lines correspond to the one-morphogen growth rule and blue to the two-morphogen growth rule. Parameters assumed as 100%: see Table S1, except growth thresholds for one-morphogen growth rule $\Theta = 0.25$, for two-morphogen growth rule $\Theta = 0.1379$, also shown in Figure S4C and D.

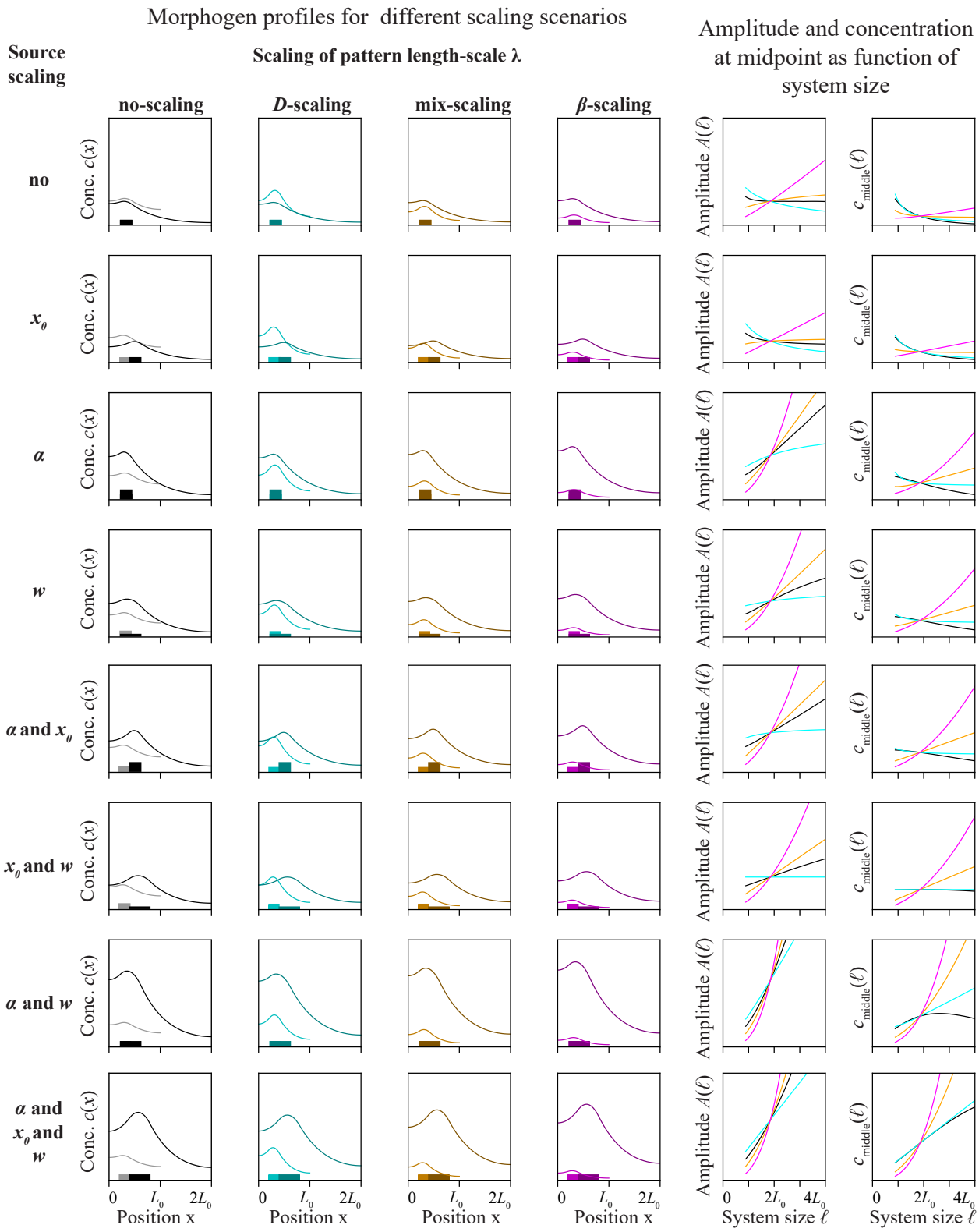

Figure S6. *Testing all scaling sub-scenarios for 5 model parameters.* The model parameters are: three parameters describing the source region, source width w, source position x_0, production rate α; and two parameters defining the pattern length-scale $\lambda = \sqrt{D/\beta}$, which can scale according D-scaling ($D \sim \ell^2$), mixed-scaling ($D \sim \ell$ and $\beta \sim 1/\ell$), and β-scaling ($\beta \sim 1/\ell^2$). The left side of the figure shows the overlaid morphogen profiles for two system sizes ℓ_0 and $2\ell_0$, (analogous to Fig. 3A) for each scaling sub-scenarios corresponding to the different combinations of source-parameter scaling (rows) and pattern length-scale-scaling (columns). The right side shows the amplitude and the concentration at the midpoint of morphogen profiles as function of system size ℓ for different scaling sub-scenarios, colored analogously to the left panel. To enable growth arrest in the case of the one-morphogen growth rule, the morphogen gradient amplitude must decay with ℓ; in the case of the two-morphogen growth rule, the morphogen concentration at the midpoint must decay with ℓ. Parameters: same as in Table S1.

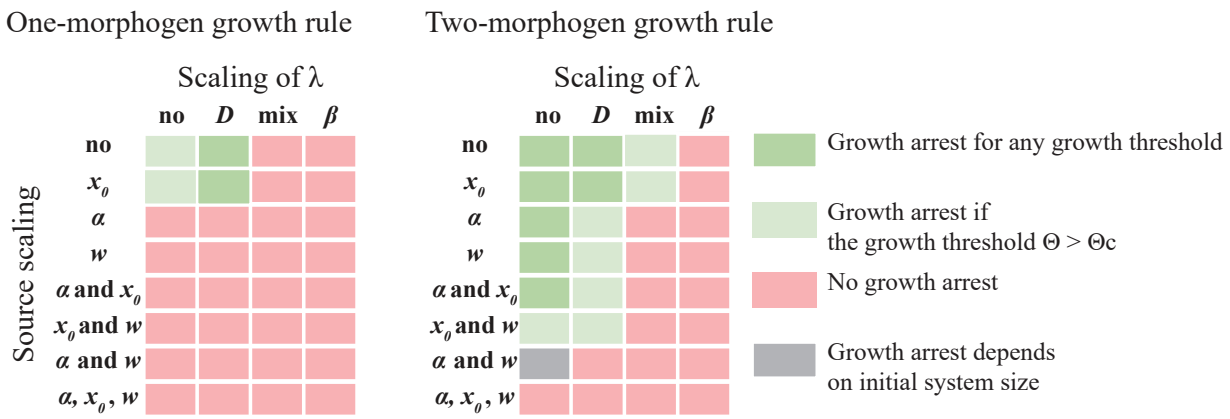

Figure S7. *Graphical summary of growth arrest for all scaling sub-scenarios for scaling of 5 model parameters for the scenario of dynamic scaling with blastema size.* Rows correspond to different combinations of source parameters (position x_0, width w, production rate α) that may scale with blastema size $L(t)$; columns correspond to different combinations of morphogen gradient parameters that may scale with $L(t)$, analogous to Fig. S6. For each sub-scenario of parameter scaling, it is indicated whether growth arrests for all choices of the growth threshold Θ (green), growth arrests if the growth threshold Θ exceeds a critical value Θ_c (light green), growth never arrests (red), or growth arrests only if the initial system size is smaller than a critical system size (gray).

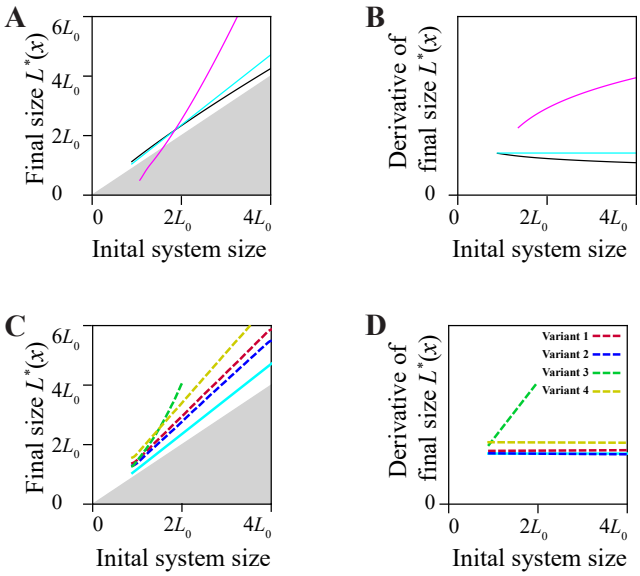

E

Parameter	Variant 1	Variant 2	Variant 3	Variant 4
w for SHH	dynamic	dynamic	dynamic	dynamic
x_0 for SHH	dynamic	dynamic	dynamic	dynamic
λ for SHH	dynamic	static	static	dynamic
w for FGF8	static	static	static	static
x_0 for FGF8	static	static	dynamic	dynamic
λ for FGF8	static	dynamic	dynamic	dynamic

	Growth arrest?
Two-morphogen	for D-scaling

	Proportional growth?		
Two-morphogen	for D-scaling	super-linearly	

Figure S8. *Proportional growth for mixed scaling scenarios.* For reference, panels A and B address scenarios of only static scaling of morphogen gradient parameters as shown in Fig. 3 in the main text, while panels C, D and E address variants of mixed scaling in which some parameters display dynamic scaling and others exhibit static scaling. *A.* Final system size as function of initial system size (assumed proportional to L_a) for three gradient scaling sub-scenarios as in Fig. 3: source scaling (black), $+D$-scaling (cyan), $+\beta$-scaling (magenta). *B.* Numerical derivative of the final system size with respect to the initial system size for the data shown in Panel A, to discriminate between sub-linear growth (decreasing), proportional growth (constant), and super-linear growth (increasing). *C.* Final system size as a function of initial system size for mixed scaling scenarios combining static and dynamic scaling (listed in panel E, assuming D-scaling; dashed), as well as the result for static scaling with D-scaling from panel A for comparison (cyan). *D.* Numerical derivative of final system size with respect to initial system size for the data shown in Panel C. *E.* Variants of mixed scaling scenarios, where some morphogen gradient parameters exhibit dynamic scaling, while other parameters exhibit static scaling. For each variant, our model predicts growth arrest and approximate proportional growth if the two-morphogen growth rule and D-scaling is assumed. Parameters: same as in Table S1, growth threshold $\Theta = 0.15$.

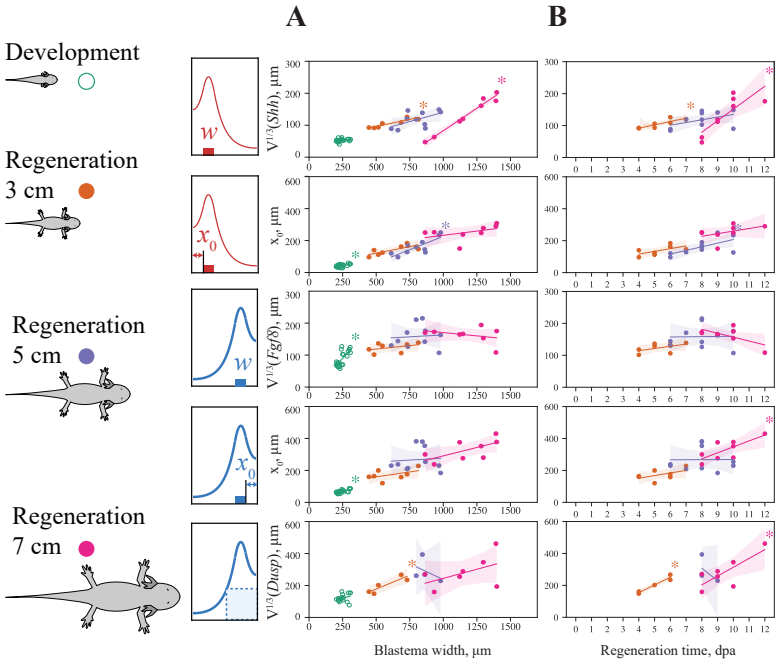

Figure S9. *Additional fit variant for Fig. 4B. A.* Same data as in Fig. 4B for experimentally measured characteristics of SHH and FGF8 source regions and signaling range, yet with separate linear regressions for each animal-size group. *B.* Same data, yet with separate linear regressions for each animal-size group plotted against regeneration time. Stars indicate that the fitted slope from linear regression is statistically significantly different from zero (p < 5%).

Parameter	Value
Diffusion coefficient D	$D_0 = 1$
Degradation rate β	$\beta_0 = 1$
Pattern length-scale λ	$\lambda_0 = \sqrt{D_0/\beta_0} = 1$
Production rate α	$\alpha_0 = 1$
Growth rate	$0.5\,\beta_0$
Source position x_0	$0.4\,\lambda_0$
Source width w	$0.4\,\lambda_0$
Initial size L_0	$1.8\,\lambda_0$
Proportionality coefficient λ/ℓ	0.3
Proportionality coefficient w/ℓ or x_0/ℓ	0.2

Table S1. *Non-dimensional parameter values used in numerical computations.* The morphogen parameters (diffusion coefficient D, degradation rate β, and production rate α) were set equal to 1; different values for these parameters correspond to trivial re-scaling of length units, time units, concentration units, and do not change any of our conclusions. The growth rate g was set to $g = 0.5\beta_0$ for most figures; other values of g are tested in Fig. S4. The source parameters (source position x_0, source width w) and proportionality coefficient assumed in morphogen gradient scaling were chosen to mimic the experimentally found values of these parameters (Fig. 4), normalized by the experimental estimate of FGF8 pattern length-scale.

	D-scaling $D \sim L^2$	Mixed-scaling $D \sim L; \beta \sim 1/L$	β-scaling $\beta \sim 1/L^2$
Amplitude	$\sim \frac{1}{L}$	Const	$\sim L$
Concentration at the midpoint	$\sim \frac{1}{L}$	Const	$\sim L$
	D-scaling $D \sim L_0^2$	Mixed-scaling $D \sim L_0; \beta \sim 1/L_0$	β-scaling $\beta \sim 1/L_0^2$
Final system size, one-morph. growth rule	$\sim$ arcoth$(C\ L_0)L_0$	$\sim L_0$	$\sim$ arcoth $\left(\frac{C}{L_0}\right) L_0$
Final system size, two-morph. growth rule	$\sim$ arcsinh$(\frac{C}{L_0})L_0$	$\sim L_0$	$\sim$ arcsinh$(CL_0)L_0$

Table S2. *Summary of analytical results.* In the limit case of a point source region, $w \to 0$, located at the left system boundary, $x_0 = 0$, the steady-state solution of the diffusion equation Eq. (1) is given by the analytical formula Eq. (S19). This table summaries how for Eq. (S19) the amplitude of the morphogen gradient profile and its concentration at the midpoint of the system depend on system size L for different sub-scenarios of dynamic scaling. Additionally, it is stated how the final system size L^* depends on the initial system size L_0 for different sub-scenarios of static scaling. Here, C denotes a constant factor that depends on the growth threshold Θ.

	Dynamic scaling?		Static scaling?	
Morphogen gradient parameter	Partial correl. analysis		Partial correl. analysis	
	η^2	p	η^2	p
w for SHH	0.21	n.s.	0.59	<0.1%
x_0 for SHH	0.02	n.s.	0.55	<0.1%
w for FGF8	0.17	0.7%	0.02	n.s.
x_0 for FGF8	0.20	0.2%	0.15	0.5%
$V^{1/3}$ for *Dusp6*	0.03	n.s.	0.2	0.9%
L_a + noise	[0.25,0.47]	[<0.1%,5%]	[-0.14,0.14]	n.s.
L + noise	[-0.14,0.14]	n.s.	[0.23,0.46]	[<0.1%,6%]

Table S3. *Partial correlation analysis for morphogen gradient parameters against animal and blastema size.* Shown are the results of a partial correlation analysis for morphogen gradient parameters as reported in Fig. 4B, which allows testing for conditional statistical independence. To test for *dynamic scaling*, we performed a partial correlation analysis against animal size, after factoring out blastema size. Here, η^2 denotes the explained residual variance of a morphogen gradient parameter due to the influence of animal size after factoring out the influence of blastema size according to Eq. S7, while p denotes the significance level of a positive linear correlation between animal size and a morphogen parameter after factoring out blastema size, computed using Eq. S10. A non-significant p-value is consistent with dynamic scaling of this parameter. To test for *static scaling*, we analogously performed a partial correlation analysis against blastema size, after factoring out animal size. Here, η^2 denotes the explained residual variance of a morphogen gradient parameter due to the influence of blastema size after factoring out the influence of animal size, and p again the significance level of the corresponding correlation. A non-significant p-value is consistent with static scaling of this parameter. For each morphogen parameter, $n = 48$ samples were analyzed, except $n = 33$ for *Dusp6*. For comparison, we applied the same test also to synthetic data comprising $n = 48$ samples with the same animal and blastema sizes as measured in the experiments, and a hypothetical parameter given by either animal size L_a or blastema size L multiplied by independent, normally distributed multiplicative noise factors with mean 1 and variance 0.25. Intervals for η^2 corresponds to the $[25\%, 75\%]$-inter quartile range.

Supplementary Note 1: Supplementary Methods

A. Numerical methods

As mentioned in the Methods section of the main text, in the presence of tissue growth with local growth rate $g(x,t)$, Eq. 1 changes to Eq. 4

$$\partial_t c(x,t) = D\,\partial_x^2 c(x,t) - \partial_x(v(x,t)c(x,t)) - [\beta + g(x,t)]c(x,t) + \alpha\,\chi_w(t)(x) \quad , \tag{S1}$$

where $\partial_x v = g$.

This equation is numerically solved using a modified Euler scheme in a Lagrangian frame. While Eulerian coordinates describe fixed coordinate positions that are stationary with respect to a fixed laboratory frame, Lagrangian coordinates describe moving coordinates that track a particular point of a flowing material such as a growing tissue and thus move with its flow. Specifically, we consider a non-uniform spatial grid with grid points $x_i(t)$ in one space dimension, whose bin sizes $\Delta x_i(t_n) = x_{i+1}(t_n) - x_i(t_n)$ change in time according to

$$\Delta x_i(t_n + 1) = [1 + g(x_i, t_n)\Delta t]\Delta x_i(t_n) \quad . \tag{S2}$$

The discretization of the Laplacian $\partial_x^2 c$ for this non-uniform grid reads

$$\partial_x^2 c(x_i,t_n) \approx \frac{2}{x_{i+1}(t_n) - x_{i-1}(t_n)} \left(\frac{c(x_{i+1},t_n) - c(x_i,t_n)}{x_{i+1}(t_n) - x_i(t_n)} - \frac{c(x_i,t_n) - c(x_{i-1},t_n)}{x_i(t_n) - x_{i-1}(t_n)} \right) \quad , \tag{S3}$$

where $c(x_i,t_n)$ is the concentration at position x_i and time t_n (more precisely, the average concentration in a spatial bin with center x_i), and x_i specifically denotes in this case the center of the spatial bin with the varying size. Note that the above Laplacian for the non-uniform grid reduces to the standard second-central-difference formula $c(x_{i+1},t_n) - 2c(x_i,t_n) + c(x_{i-1},t_n)/\Delta x^2$ if the grid spacing is uniform $x_{i+1}(t_n) - x_i(t_n) = x_i(t_n) - x_{i-1}(t_n) = \Delta x$. For the diffusion equation Eq. 4, the numerical Euler step reads

$$c_i^{n+1} = c_i(t_n) \; - \Delta t\; (\beta + g)c_i(t_n) \; + \Delta t\; D \frac{2}{x_{i+1} - x_{i-1}} \left(\frac{c_{i+1}(t_n) - c_i(t_n)}{x_{i+1} - x_i} - \frac{c_i(t_n) - c_{i-1}(t_n)}{x_i - x_{i-1}} \right) + \Delta t\; \alpha\,\chi_w(x_i) \quad . \tag{S4}$$

B. Image analysis

First, all 3D images were re-binned for isotropic voxel size with dimensions $2 \times 2 \times 2$ μm, then rotated and cropped in 3D with Napari Chiu et al. (2022). Blastemas were segmented using APOC Haase et al. (2023), trained with user-specified ground truth labels marking the tissue and the outside areas, respectively, and applied to the *Shh* channel. A constant background, corresponding to the mean intensity outside the segmented blastema, was subtracted from each channel. The blastema contained a significant number of blood cells, resulting in imaging artifacts across all channels. To address this issue, autofluorescence was acquired (499-nm illumination), and APOC segmentation was applied to this channel to identify a binary blood-vessel mask, which was subsequently excluded from all channels. Additionally, for some images, the intensity of the *Shh* channel decayed significantly along the z-axis. This artifact was corrected by normalizing the *Shh* intensity along the axis using the intensity profile calculated at the most anterior edge of the tissue, outside the possible *Shh* region.

The *Shh*, *Fgf8*, and *Dusp6* channels were denoised using a 3D Gaussian blur with a standard deviation of 10 μm (5 pixels), followed by min-max normalization. The SHH and FGF8 source regions, as well as the FGF8 signaling range region indicated by *Dusp6* mRNA in 3D, were determined as regions enclosed by the respective 50%-iso-intensity surfaces. Small disconnected components were manually removed from the volumes enclosed by these iso-intensity surfaces. The linear size of these regions were determined as the cubic roots of the volumes enclosed by the respective surfaces. Choosing different iso-intensity surfaces, i.e., at 40% or 60% relative intensity, gave the same qualitative conclusions about scaling as Fig. 4.

Blastema size was measured in 3D images along a line passing through the centers-of-mass of the *Shh* and the *Fgf8* regions, as indicated in Fig. 4A, inset. We will refer to this line as SF in the following. At late stages of development and regeneration, the *Fgf8* region starts to attain a non-convex shape, and eventually splits into two separate domains. To determine the gap (x_0) between the tissue boundary and the boundary of the *Shh* and *Fgf8* regions in a robust manner, even for non-convex shapes of source regions, we first projected the three-dimensional binary masks along the dorsal-ventral axis onto a 2D-plane (using a logical OR-operation along the projection axis). Here, the dorsal-ventral axis was determined as the axis among all axes perpendicular to the line SF that was maximally aligned to the principal axis with smallest singular value obtained by a principal-component analysis (PCA) of the binary mask of the limb bud or blastema. The outlines of these projections are shown in Fig. 4A. We

then measured the distance x_0 between the tissue boundary and the boundary of each source region in this 2D projection along the line SF. For the visualization in Fig. 4, 2D-projections of different samples corresponding to the same animal size and time-point were aligned by registering the midpoint and orientation of the line segment $\overline{SF}$ connecting the centers-of-mass S and F of the *Shh* and *Fgf8* regions. Limb buds stages were assigned as introduced in Nye et al. (2003).

C. Experimental Methods

Animal breeding. Larval axolotls (*Ambystoma mexicanum*) were maintained at the axolotl facility at CRTD TU Dresden as described Khattak et al. (2014). Optimized axolotl (*Ambystoma mexicanum*) husbandry, breeding, metamorphosis, transgenesis and tamoxifen-mediated recombination were applied as in Khattak et al. (2014). All procedures were performed according to the Animal Ethics Committee of the State of Saxony, Germany. Animals of the d/d genetic backgrounds with body length in the range 1.2-9 cm were used for the HCR staining. For live measurements of blastema size, axolotls of the ZRS>TFP background (tgSceI(ZRS:TFPnls-T2A-ERT2-Cre-ERT2)^{Etnka} Otsuki et al. (2023) with body length in the range 1.2-25 cm length were used.

Limb amputation and tissue collection Axolotls were anesthetized in 0.01% benzocaine solution for approximately 20 minutes. Sleeping animals were placed on a clean Petri dish to image and measure the size of the limb. Limbs were amputated using a scalpel such that the distal quarter of the zeugopod was removed and the protruding radius and ulna were trimmed with scissors to create a flat surface. To monitor the progress of regeneration, the animals were again anesthetized in 0.01% benzocaine and imaged using a SZX16 wide field microscope with bright field illumination or UV light for the ZRS>TFP line to visualize the expression of TFP protein. Prior to tissue collection, the animals were anesthetized and limbs were imaged to record the blastema stage. For staining, limbs were cut off at the shoulder level and fixed in MEMFA (0.1 M MOPS pH 7.4, 2 mM EGTA, 1 mM MgSO4·7H2O and 3.7% formaldehyde) for at least 3 days at 4°C. For qPCR, only blastema and a sliver of 0.5-1 mm of tissue behind the amputation plane were collected, immediately frozen in liquid nitrogen and kept at -70°C until use.

Whole-mount HCR *in situ* hybridization and tissue clearing. Target transcripts were identified in the axolotl transcriptome Amex.T_v47 Schloissnig et al. (2021) and confirmed by BLASTX alignment to the NCBI Refseq Protein Database. HCR probe pairs were designed by the `https://probegenerator.herokuapp.com/` probe generator, which uses Bowtie2 Langmead and Salzberg (2012) to exclude probes that hit multiple genomic regions in the 60DD axolotl genome. Probe pairs (30-40 per target transcript) were ordered as oPools from Integrated DNA Technologies. Other consumables, including hybridization, wash and amplification buffers, as well as HCR hairpins were purchased from Molecular Instruments. RNA staining was done using the whole-mount HCR protocol from Choi et al. (2018) with the following modifications. Tissues were collected and fixed in MEMFA (3.7% formaldehyde in MEM buffer) for >3 days at 4°C. Fixative was washed out by 3 × 15 minute washes in PBST (PBS +0.1% Tween), dehydrated with 25%, 50%, and 75% MeOH in PBST all on ice and finally stored at -20°C until use (up to 2 years). After re-hydration, the permeabilization step using Proteinase K was omitted and replaced by delipidation in boric acid buffer (200 mM boric acid, 4% SDS at pH8.5) for 2-4 h at room temperature, and permeabilization in 2% TritonX-100, 0.3M glycine, 20% DMSO in PBS either at 20°C or 37°C, for 12-14h. In the detection step, the initiator pools for all target genes of interest were combined, with the concentration of each initiator pool in the hybridization solution increased to 20 nM and the reaction extended to 20 h. In the signal amplification step, Alexa-546, Alexa-647 and Alexa-750 conjugated hairpins were used at 60 nM each to detect Fgf8, Dusp6 and Shh mRNA, respectively. Both the detection and amplification steps were extended to 20-24 h. Following the final washes of the amplification step, nuclei were stained by incubation in 5xSSCT with DAPI (4,6-diamidino-2-phenylindole Sigma, #D9542) overnight at 4°C. For sample clearing, first, an equal amount of EasyIndex RI 1.52 (LifeCanvas Technologies) was added for 1 day at 4°C. Limbs were glued into a homemade vessel and covered with 100% EasyIndex for 3-10 days prior to imaging. All incubation steps were performed on a shaker or rocker. In all steps following the addition of the amplifiers, the samples were protected from light.

Whole-mount imaging. The whole-mount imaging was performed using an upright laser scanning confocal microscope Stellaris 8 (Leica) with a long range pulsed white light laser (flexible range 440-790 nm) and a pulsed 405-nm laser. For detection, LAS X software and a HC FLUOTAR L 16x/0,60 IMM CORR VISIR (11506533) Mag=16x, NA=0.6, WD=2.5mm, objective were used. The detection objective was set to match the RI of the clearing media (1.52) prior to imaging. HCR signal of Fgf8, Shh and Dusp6 was detected using the 557-nm, 752-nm and 653-nm excitation wavelength lasers. 499-nm illumination was used to detect autofluorescence. DAPI was illuminated with the 405-nm laser.

qPCR. RNA for RT–PCR was purified using RNeasy Mini Kit (Qiagen Cat. No. 74104). Reverse transcription was performed using SuperScript™ IV Reverse Transcriptase (Invitrogen^{TM}, Can. No.15387686) and Oligo dT17V as

a primer. The quantitative PCR was performed using TB Green® Premix Ex Taq^{TM} (Tli RNase H Plus) kit (Takara, Cat. No. RR420L).
The following primers were used:

Target gene	Forward	Reverse
Fgf8	829 CCGCATTAAAGGAGCCGAGA	830 ATGAGGCTCCGTTGTTTGGT
Dusp6	340 CCAGGACTGTCTCAAAGATTCTGC	341 GCCTTCCGCAAGCATACATTG
Shh	806 GCTCTGTGAAAGCAGAGAACTCG	807 CGCTCCGTCTCTATCACGTAGAA
Ptch1	802 CGATCGAGAAAGTGAGGGCCATA	803 GAACTCCACTCCAATGCCAACAG
Grem1	813 GAGAGACCACACATGCCTGAA	814 GGAGGTGGAAGAGATGTGCAA
Rlp4	185 TGAAGAACTTGAGGGTCATGG	186 CTTGGCGTCTGCAGATTTTTT

Analysis was performed for two biological replicates. The parallel processing of samples should make individual normalized mRNA concentrations comparable for the two animal sizes.

D. Statistical Methods

Unweighted linear regressions by least-square-fit for slope and intercept were performed for Figs. 1C, 4B. Statistical significance of non-zero slope indicated by a star in Fig. 4B was determined by two-sided t-test at confidence level $\alpha = 0.05$. Fig. 4B, second column, shows linear regressions against animal size L_a. For each morphogen gradient parameter, a linear regression was performed against the animal size of individual samples; for visualization, a constant was computed for each size group using this linear regression and the average animal size in each size-group.
To test for *dynamic scaling* versus *static scaling* of SHH and FGF8 morphogen gradient parameters, a partial correlation analysis was performed on the data presented in Fig. 4B as follows. Let the observable X denote a morphogen gradient parameter. The statistical factors animal size $Y = L_a$ and blastema size $Z = L$ may both influence X. If X exhibits dynamic scaling, X should strongly correlate with Z, yet will be also correlated with Y because Y and Z are correlated. To factor out the effect of Z, we first performed separate linear regressions

$$X_i = \alpha_X + \beta_X Z_i + \varepsilon_{X,i} \text{ and } Y_i = \alpha_Y + \beta_Y Z_i + \varepsilon_{Y,i} \quad , \tag{S5}$$

where $i = 1, \ldots, n$ enumerates the samples, and $\varepsilon_{X,i}$ and $\varepsilon_{Y,i}$ denote the respective residuals for X and Y. Next, we perform a linear regression between these residuals to reveal effects of Y on X not yet explained by Z

$$\varepsilon_{X,i} = \alpha + \beta \varepsilon_{Y,i} + \varepsilon_i \quad . \tag{S6}$$

The fraction η^2 of residual variance of X explained by Y after factoring out Z reads

$$\eta^2 = 1 - \frac{\sum_{i=1}^n \varepsilon_i^2}{\sum_{i=1}^n \varepsilon_{X,i}^2} \quad . \tag{S7}$$

The statistical significance of the effect of Y on X after factoring out Z can be tested as follows. Let r_{AB} denote the correlation coefficient between two variables A and B (Bravais-Pearson correlation)

$$r_{AB} = \frac{\sum_{i=1}^n (A_i - \overline{A})(B_i - \overline{B})}{\sqrt{\left(\sum_{i=1}^n (A_i - \overline{A})^2\right)\left(\sum_{i=1}^n (B_i - \overline{B})^2\right)}} \quad , \tag{S8}$$

where $\overline{A}$ and $\overline{B}$ denote the sample means of A and B, respectively. The *partial correlation coefficient* $r_{XY,Z}$ between X and Y after factoring out Z is then given by Rudolf and Kuhlisch (2008)

$$r_{XY,Z} = \frac{r_{XY} - r_{XZ} r_{YZ}}{\sqrt{\left(1 - r_{XZ}^2\right)\left(1 - r_{YZ}^2\right)}} \quad . \tag{S9}$$

If the null hypothesis that Y has no effect on X after factoring out Z is true (and errors are independent and distributed normally with equal variance), the derived test-variable $t_{XY,Z}$ obeys a t-distribution with $n-3$ degrees of freedom

$$t_{XY,Z} = \sqrt{n-3} \frac{r_{XY,Z}}{\sqrt{1 - r_{XY,Z}^2}} \quad . \tag{S10}$$

Now, p-values of a one-sided t-test can be readily computed. To test if a morphogen gradient parameter X exhibits static scaling, the above analysis can be repeated with the roles of Y and Z swapped. Results are reported in Table S3. The data reported in Fig. 4b is thus compatible with dynamic scaling of source region size w and source position x_0 for SHH, and static scaling of source region size w for FGF8.

Supplementary Note 2: Supplementary Information for Mathematical Modeling

A. Steady-state solutions of diffusion equation

Finite system size and extended source region. We recall Eq. (1) from the main text

$$\partial_t c(x,t) = D\partial_x^2 c(x,t) - \beta c(x,t) + \alpha\chi(x) \quad . \tag{S11}$$

We assume reflection boundary conditions, i.e., no flux of morphogens at the system's boundaries $x=0$ and $x=L$

$$\partial c_x(x)|_{x=0} = \partial c_x(x)|_{x=L} = 0 \quad . \tag{S12}$$

At steady state, 1 reduces to

$$0 = \lambda^2\partial_x^2 c(x,t) - c(x,t) + \frac{\alpha}{\beta}\chi(x) \quad , \tag{S13}$$

where $\lambda = (D/\beta)^{1/2}$ denotes the pattern length-scale as introduced in the main text. The Green's function for the differential operator $\lambda^2\partial^2 - 1$ with reflective boundary conditions Eq. (S12) reads

$$G(x,s) = \frac{1}{\lambda \sinh\frac{L}{\lambda}}\left[\cosh\left(\frac{L-s}{\lambda}\right)\cosh\left(\frac{x}{\lambda}\right)\Theta(s-x) + \cosh\left(\frac{s}{\lambda}\right)\cosh\left(\frac{L-x}{\lambda}\right)\Theta(x-s)\right] \quad , \tag{S14}$$

where $\Theta(x)$ denotes the Heaviside step function. Thus, the steady state solution c^* of Eq. (1) can be written for an arbitrary source region described by a shape function $\chi(x)$ as

$$c^*(x) = \frac{\alpha}{\beta}\int_0^L G(x,s)\,\chi(s)\,ds \quad . \tag{S15}$$

For the source function introduced in the main text

$$\chi_w(x) = \Theta(w+x_0-x)\Theta(x-x_0) \quad , \tag{S16}$$

which takes the constant value 1 inside the interval $[x_0, x_0+w]$ and zero outside, the steady state solution c^* reads

$$c^*(x) = \frac{\alpha}{\beta\sinh\frac{L}{\lambda}}\begin{cases} 2\sinh\frac{w}{2\lambda}\cosh\frac{2L-(w+2x_0)}{2\lambda}\cosh\frac{x}{\lambda}, & x\in(0,x_0) \\ \sinh\frac{L}{\lambda} - \left(\sinh\frac{L-w-x_0}{\lambda}\cosh\frac{x}{\lambda} + \sinh\frac{x_0}{\lambda}\cosh\frac{L-x}{\lambda}\right), & x\in[x_0,x_0+w] \\ 2\sinh\frac{w}{2\lambda}\cosh\frac{w+2x_0}{2\lambda}\cosh\frac{L-x}{\lambda}. & x\in(x_0+w,L) \end{cases} \tag{S17}$$

Point source region. To facilitate analytical analysis of growth arrest and morphogen gradient scaling as function of key model parameters (diffusion coefficient D, degradation rate β, and total production rate $j=\alpha w$), we state the steady-state solution of Eq. (S17) for a point morphogen source region located at $x=x_0$, corresponding to the limit $w\to 0$ with $j=\alpha w=$ const.

$$c^*(x) = \frac{\alpha w}{\sqrt{D\beta}\sinh\frac{L}{\lambda}}\begin{cases} \cosh\frac{L-x_0}{\lambda}\cosh\frac{x}{\lambda}, & x\in(0,x_0] \\ \cosh\frac{x_0}{\lambda}\cosh\frac{L-x}{\lambda}. & x\in(x_0,L) \end{cases} \tag{S18}$$

Point source region at system boundary. For sake of completeness, we additionally state the steady-state solution of 1 for a point source located the the system boundary $x_0=0$

$$c^*(x) = \frac{\alpha w}{\sqrt{D\beta}\sinh\frac{L}{\lambda}}\cosh\frac{L-x}{\lambda} \quad . \tag{S19}$$

As a technical point, the no-flux boundary condition S12 needs to be modified for a point source located at the system boundary such that the diffusive flux equals morphogen production, $-D\partial_x c_{|x=0} = j$.

Point source region in an unbounded system. In the limit of an unbounded system with $L\to+\infty$, the steady-state solution S19 further simplifies to

$$c^*(x) = \frac{\alpha w}{\sqrt{D\beta}}\exp\left(-\frac{x}{\lambda}\right) \quad , \tag{S20}$$

corresponding to Eq. (3) in the main text.

B. Oppositely-oriented morphogen gradients at left and right system boundaries

As mentioned in main text, the degradation-diffusion model for morphogen dynamics Eq. (1) can be generalized in a straight-forward manner to the case of two opposing morphogen gradients with respective concentration fields $s(x,t)$ and $f(x,t)$, which can be explicitly written as

$$\partial_t s(x,t) = D\,\partial_x^2 s(x,t) - \beta\, s(x,t) + \alpha\,\chi_s(x) \quad , \tag{S21}$$

$$\partial_t f(x,t) = D\,\partial_x^2 f(x,t) - \beta\, f(x,t) + \alpha\,\chi_f(x) \quad , \tag{S22}$$

where, for simplicity, the source regions are also mirror-symmetric, $\chi_s(x) = \chi_f(L-x)$.

C. Growth rules define the final system size as function of model parameters

One-morphogen growth rule. In the case of the one-morphogen growth rule, growth stops when the growth threshold Θ equals the morphogen gradient amplitude A. The final system size L^* is thus determined by the condition

$$L^*_{\text{one}} : A := \max_{[0,L^*]} c(x) \stackrel{!}{=} \Theta \quad . \tag{S23}$$

In the limit case of a point morphogen source Eq. S19, the final system size can be written as

$$L^*_{\text{one}} = \lambda \text{ arcoth}\left(\frac{\Theta\sqrt{D\beta}}{\alpha w}\right) \quad . \tag{S24}$$

The function arcoth $\left(\frac{\Theta\sqrt{D\beta}}{\alpha w}\right)$ is defined only for $\frac{\Theta\sqrt{D\beta}}{\alpha w} > 0$, which gives the critical growth threshold Θ_{cr} for growth arrest for the one-morphogen growth rule as

$$\Theta_{\text{cr}} = \frac{\alpha w}{\sqrt{D\beta}} \quad . \tag{S25}$$

Two-morphogen growth rule. For the two-morphogen growth rule, growth stops when the growth threshold Θ equals the morphogen concentration at the intersection of the morphogen. For simplicity, we consider the symmetrical case, where both morphogens have identical parameters, but their source regions are located at opposite boundaries of the system. In this case, morphogen gradients intersect at the midpoint of the system; therefore, the final system size L^* is determined by

$$L^*_{\text{two}} : c\left(\frac{L^*}{2}\right) \stackrel{!}{=} \Theta \quad . \tag{S26}$$

In the limit case of point morphogen source, Eq. S19, the final system size can be written as

$$L^*_{\text{two}} = 2\lambda \text{ arcsinh}\left(\frac{\alpha w}{2\Theta\sqrt{D\beta}}\right) \quad . \tag{S27}$$

D. Mutual feedback between morphogens

In the main text, we introduced feedback between the two morphogens, where a morphogen can only be produced inside a competent zone at the boundary with width $w_{\text{competent}}$ if the other morphogen exceeds a fixed feedback threshold, Θ_{fb}. To obtain the phase diagram Fig. 5B, we define a separatrix that separates a regime dominated by the growth threshold Θ and a regime dominated by the feedback threshold Θ_{fb}. Specifically, the separatrix is defined by the condition that both thresholds can be reached simultaneously. Accordingly, the final source position x_0^* is both strictly positive and strictly smaller than $w_{\text{competent}}$.

In our minimal model, growth arrests only if the growth threshold Θ has been reached. For the two-morphogen growth rule, this occurs at the midpoint of system, see also Eq. S26. In this case, the source width equals $w_{\text{competent}} - x_0^*$. Hence, assuming that the growth threshold is reached outside the source region and using Eqs. S17 and S26, the growth threshold can be explicitly written as

$$\Theta = \frac{2\alpha}{\beta \sinh\left(\frac{L^*}{\lambda}\right)} \sinh\left(\frac{w_{\text{comp.}} - x_0^*}{2\lambda}\right) \cosh\left(\frac{2w_{\text{comp.}} + x_0^*}{2\lambda}\right) \cosh\left(\frac{L^*}{2\lambda}\right) \quad . \tag{S28}$$

For the case of symmetrical morphogens at two opposing sides of the system, we can also state the feedback threshold at the moment of growth arrest as the concentration at the position $x = L^* - x_0^*$, which can be written as

$$\Theta_{\text{fb}} = \frac{2\alpha}{\beta \sinh\left(\frac{L^*}{\lambda}\right)} \sinh\left(\frac{w_{\text{comp.}} - x_0^*}{2\lambda}\right) \cosh\left(\frac{2w_{\text{comp.}} + x_0^*}{2\lambda}\right) \cosh\left(\frac{x_0^*}{\lambda}\right) \quad . \tag{S29}$$

Assuming the critical situation, where $x_0^* = 0$ and varying the final system size L^* according to Eq. S28 and Eq. S29, we obtain the separatrix between the two regimes as shown in Fig. 5B.

References

Chiu, C.-L., Clack, N., et al. (2022). Napari: a python multi-dimensional image viewer platform for the research community. *Microscopy and Microanalysis*, 28(S1):1576–1577.

Choi, H. M., Schwarzkopf, M., Fornace, M. E., Acharya, A., Artavanis, G., Stegmaier, J., Cunha, A., and Pierce, N. A. (2018). Third-generation in situ hybridization chain reaction: multiplexed, quantitative, sensitive, versatile, robust. *Development*, 145 (12):dev165753.

Haase, R., Lee, D., Pop, D. D., and Žigutytė, L. (2023). haesleinhuepf/napari-accelerated-pixel-and-object-classification: 0.14. 1. *Zenodo https://doi. org/10.5281/zenodo*, 10071078.

Khattak, S., Murawala, P., Andreas, H., Kappert, V., Schuez, M., Sandoval-Guzmán, T., Crawford, K., and Tanaka, E. M. (2014). Optimized axolotl (ambystoma mexicanum) husbandry, breeding, metamorphosis, transgenesis and tamoxifen-mediated recombination. *Nature protocols*, 9(3):529–540.

Langmead, B. and Salzberg, S. L. (2012). Fast gapped-read alignment with bowtie 2. *Nature methods*, 9(4):357–359.

Nye, H. L., Cameron, J. A., Chernoff, E. A., and Stocum, D. L. (2003). Extending the table of stages of normal development of the axolotl: limb development. *Developmental dynamics: an official publication of the American Association of Anatomists*, 226(3): 555–560.

Otsuki, L., Plattner, S. A., Taniguchi-Sugiura, Y., and Tanaka, E. M. (2023). Molecular basis for positional memory and its reprogrammability in limb regeneration. *bioRxiv*, pages 2023–10.

Rudolf, M. and Kuhlisch, W. *Biostatistik: Eine Einführung für Biowissenschaftler*. Cambridge University Press, (2008).

Schloissnig, S., Kawaguchi, A., Nowoshilow, S., Falcon, F., Otsuki, L., Tardivo, P., Timoshevskaya, N., Keinath, M. C., Smith, J. J., Voss, S. R., et al. (2021). The giant axolotl genome uncovers the evolution, scaling, and transcriptional control of complex gene loci. *Proceedings of the National Academy of Sciences*, 118(15):e2017176118.